Ab initio molecular dynamics calculations on reactions of molecules with metal surfaces

Nattino, F.

Chapter 4

Dissociation and Recombination of D_2 on Cu(111): *Ab initio* Molecular Dynamics Calculations and Improved Analysis of Desorption Experiments

This chapter is based on:

F. Nattino, A. Genova, M. Guijt, A. S. Muzas, C. Díaz, D. J. Auerbach and G. J. Kroes, J. Chem. Phys. **141**, 124705 (2014).

Abstract

Obtaining quantitative agreement between theory and experiment for dissociative adsorption of hydrogen on and associative desorption of hydrogen from Cu(111) remains challenging. Particularly troubling is the fact that theory gives values for the high energy limit to the dissociative adsorption probability that are as much as two times larger than experiment. In the present work we approach this discrepancy in three ways. First, we carry out a new analysis of the raw experimental data for D_2 associatively desorbing from Cu(111). We also perform new *ab initio* molecular dynamics (AIMD) calculations

that include effects of surface atom motion. Finally, we simulate time-of-flight (TOF) spectra from the theoretical reaction probability curves and we directly compare them to the raw experimental data. The results show that the use of more flexible functional forms for fitting the raw TOF spectra gives fits that are in slightly better agreement with the raw data and in considerably better agreement with theory, even though the theoretical reaction probabilities still achieve higher values at high energies. The mean absolute error (MAE) for the energy E_0 at which the reaction probability equals half the experimental saturation value is now lower than 1 kcal/mol, the limit that defines chemical accuracy, while a MAE of 1.5 kcal/mol was previously obtained. The new AIMD results are only slightly different from the previous static surface results and in slightly better agreement with experiment.

4.1 Introduction

Heterogeneously catalyzed processes, which are composed of sequences of elementary molecule-surface reactions, are widely employed in the industrial production of many important chemicals. Despite the relevance of the field, even the simplest elementary reactions on metal surfaces like the dissociation of the smallest molecule, H_2, on metals remains challenging to model quantitatively [1]. In this framework, the dissociative chemisorption of H_2 on copper surfaces is ideal for testing the accuracy of dynamical models and electronic structure calculations, as evidence exists that it is essentially electronically adiabatic [2–4]. Furthermore, working on this benchmark for activated chemisorption is advantageous due to the large number of experimental [5–21] and theoretical [22–47] studies available for comparison. In surface chemistry, the H_2 + Cu(111) reaction [8,11,12,19,26,39,43] has a status that is similar to that of the H_2 + H exchange reaction [48–54] in gas phase chemistry, major challenges to theorists being to explain the associated chemical physics and to demonstrate the validity of their methods for the system concerned.

A previous theoretical study [39, 40] based on the Born-Oppenheimer and static-surface approximations (BOSS) reached chemical accuracy (errors $\leq$ 1 kcal/mol) in the

description of many sets of experimental data for H_2 and D_2 on Cu(111). Electronic structure calculations were performed using density functional theory (DFT) with a semi-empirical density functional, developed according to the specific reaction parameter (SRP) approach originally developed by Truhlar and coworkers for gas-phase reactions [55, 56]. Nevertheless, a quantitative description of some experimental observables, like the rotational quadrupole alignment parameter ($A_2^{(0)}$) [19], the probability of vibrational excitation [14] and the influence of the initial rovibrational state of D_2 on the reactivity [13], was not yet achieved.

Data on the initial state-resolved reaction probability of D_2 on Cu(111) were obtained from post-permeation associative desorption experiments [13, 19], in which D atoms were supplied to the surface through permeation of the bulk. The experiments used a high surface temperature (T_s = 925 K) in order to have a sufficient flux of permeating atoms. The quantum state of the desorbing molecules was probed via laser excitation using resonance-enhanced multiphoton ionization (REMPI) [57], and their translational energy distribution was determined from time-of-flight (TOF) measurements of the ions through a field free region.

In previous theoretical work, the failure of the BOSS study in describing $A_2^{(0)}$ was attributed to the static surface approximation employed, considered unable to describe this observable measured at high surface temperature [39, 40]. The effect of phonons on the reactivity of H_2 on Cu(111) was first modeled in a very approximate way [40], using the surface oscillator model [58, 59], but this was insufficient to account for the discrepancies in $A_2^{(0)}$ between theory and experiment. The fact that the measured initial-state-selected effective barrier heights ($E_0(v, J)$) of H_2 could be accurately reproduced using the BOSS model, even though the experiments were performed at high surface temperature, can be explained on the basis of observations according to which $E_0(v, J)$ should be independent of surface temperature effects. It has been shown that varying only the width of the reaction probability curve is sufficient to account for most of the surface temperature effects on reaction [21]. Despite the good agreement obtained for H_2, a larger mean absolute error (MAE) was obtained for D_2 in the description of

$E_0(v, J)$ (1.48 kcal/mol) [39].

More recently, *ab initio* molecular dynamics (AIMD) has been used to introduce the motion of the surface atoms in the calculations and to model the effect of the experimental surface temperature (Ref. [43] and Chapter 3). The results showed that modeling surface temperature effects substantially improves the agreement between theory and experiment for the rotational alignment parameter, and slightly improves the agreement for the reaction probability of the two initial rovibrational states investigated. Wijzenbroek and Somers developed the so-called static corrugation model (SCM), in which the 'static' effects of surface temperature, i.e. of the thermal lattice expansion and of the thermal distribution of the displacements of the surface atoms from their equilibrium positions, were simulated [44]. Their results, which showed that modeling surface temperature with the SCM affects the reaction probability curves through both a small shift in energy and a 'broadening' of the curves, are in better agreement with experimental data than the BOSS results, and in good agreement with AIMD.

As alternative to dynamical models, Harrison and coworkers proposed a dynamically-biased microcanonical model, in which a limited number of adjustable parameters are fitted to an experimental set of data sensible to the dynamical biases part of the model [47]. This semi-empirical model was able to accurately describe a large variety of experimental data, over a large range of collision energies, but it may be argued that this was done to some extent by simply fitting the vibrational and rotational efficacies to experiment. The model also gave a good description of the surface temperature dependence of the state-specific reaction probability curves extracted from TOF data by Murphy and Hodgson [21]. However, such a microcanonical model is still limited in which 'dynamical' experimental observables can be computed (for instance, the rotational alignment parameter, or the vibrational excitation probability cannot be computed with the present model). On the other hand, our dynamical model for H_2 + Cu(111) can be systematically improved by adding more (phonon) degrees of freedom, and describing these more accurately, while the SRP density functional we developed is firmly rooted in a validation against observables either measured at low surface temperature (sticking probability

determined via molecular beam experiments, data on rotationally inelastic scattering) or against observables that experiments suggest to exhibit no, or little, dependence on surface temperature ($E_0(v, J)$). Our model is best suited to describing the reactivity at the (111) terraces, which should dominate the reactivity of the surfaces defined by accurately cut crystals for the higher translational energies considered in our study (close to E_0). Such conditions are presently best for validating electronic structure theory for highly activated molecule-surface reactions [60], as the presence of defects, of which there may be an ill-defined variety [61], would strongly affect the thermal reactivity of molecules on metal surfaces [62, 63]. We consider the dynamically biased microcanonical theory currently less useful for such validation purposes, as it produces a zero-point energy corrected reaction threshold value for which comparison of electronic structure theory to experiment through rate theory might lead to ambiguous results for highly activated reactions.

In the current work we tackle some of the significant discrepancies that still exist between dynamical models and experiments. For instance, both the BOSS and the AIMD models mentioned above overestimate the experimental D_2 reaction probabilities at the high collision energies (see Figure 4.1). Also, in contrast to theory the experimental maximum reaction probability showed a strong dependence on v [13, 15], the value for $v = 1$ exceeding the $v = 0$ value by a factor 1.85. Furthermore, the BOSS model has a MAE in the description of $E_0(v, J)$ which is considerably larger for D_2 than for H_2 [39], as mentioned earlier. Moreover, theory is slightly shifted to lower energies (20-40 meV) compared to the highest nozzle temperature sticking probability curve determined via molecular beam experiments [11]. In contrast, the theoretical initial state-selected reaction probabilities are shifted towards higher energies by about 50-100 meV compared to the experimental curves [39, 40], the shift being the largest for $v = 0$ and $v = 1$ D_2. Finally, the state-averaged average desorption energy computed from the experimental reaction probability curves is 71 meV lower than the value measured by Comsa and David [64], considered to be the most accurate measurement of this observable, as discussed by Sementa et al. [65].

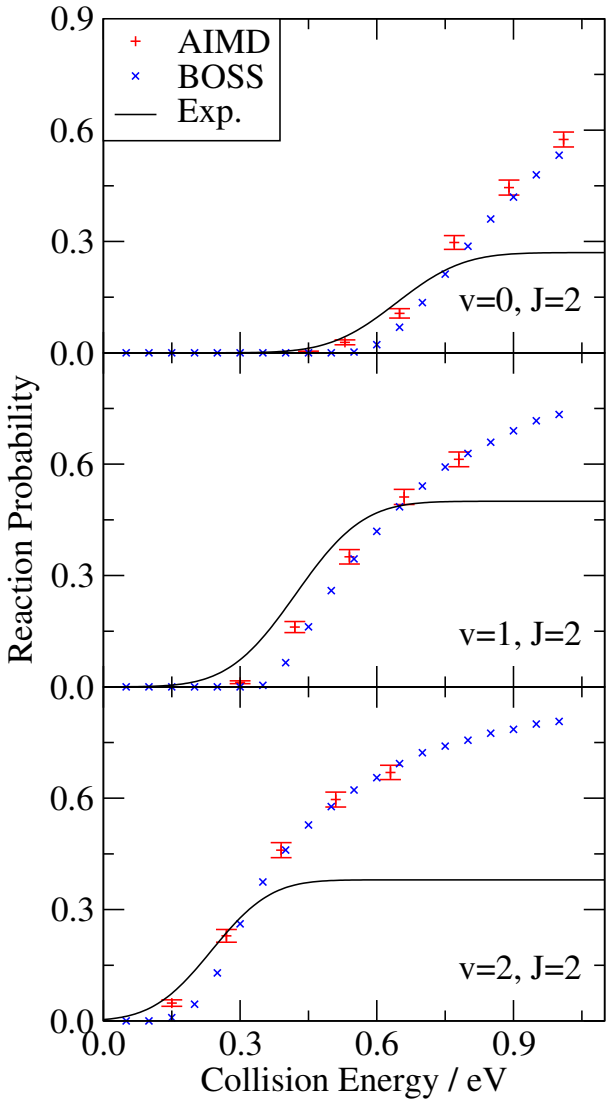

Figure 4.1: Initial-state-selected reaction probability curves for three representative states: ($v = 0, 1, 2; J = 2$). Black curve: experimental data from Ref. [13]. Blue ×: BOSS results from Refs. [39, 40]. Red +: AIMD data.

Here, we present four approaches to resolving these discrepancies and inconsistencies. First, we re-examined the raw TOF data from associative desorption experiments [13] to see if the form of the initial-state-selected reaction probability curve ($S_{v,J}(E)$) used to fit the data might be responsible for the discrepancies in $S_{v,J}$ at high incidence energy. In particular, more flexible sigmoid functions than the traditionally used error function (ERF) have been tested in modeling the reaction probability curves when fitting the TOF spectra. The choice to also test asymmetric sigmoid functions was motivated by the outcome of calculations with the hole model [66, 67], of which results are also presented here. Second, in the fits of the TOF spectra, we have used an expression for the influence of the angle with which the molecule leaves the surface on its TOF that is more accurate than the one used before [13]. Note that the choice of fitting function is also relevant to activated reactions other than H_2 + Cu(111) [13,16], such as N_2+W(110) [68], CH_4+Pt(111) [69], CH_4+Ni(111) [70] and H_2O+Ni(111) [71], which have all been modeled with the ERF form. Third, we have extended the number of initial rovibrational states of D_2 investigated with AIMD, and compare these new AIMD results both to the previous BOSS data and to the newly-fitted experimental reaction probabilities. Finally, we have simulated TOF spectra from the computed reaction probabilities, to achieve a more direct comparison between the theoretical results and experimental raw data, without any manipulation of the latter other than the background subtraction. To our knowledge, this is the first time that TOF data describing associative desorption are simulated directly on the basis of computed dissociative chemisorption probabilities.

We find that the choice of the functional form employed for the reaction probability curve when fitting an experimental TOF spectrum strongly influences the saturation value of the experimental reaction probability curves for $v = 0$. However, the new analysis does not fully solve the discrepancies between theoretical and experimental saturation values, and theoretical reaction probabilities are still larger than the experimental values at high energies. Furthermore, due to corrections to the method of doing angular averaging in the analysis of the TOF spectra, the experimental reaction probability curves are now slightly shifted to higher collision energies, improving the agreement between

theory and experiment in the $E_0(v, J)$ value: the MAE of experiment relative to both BOSS and AIMD is now lower than 1 kcal/mol, the limit which conventionally defines 'chemical accuracy'. Compared to the BOSS model, the AIMD method produces reaction probability curves which are in most cases slightly broader and slightly shifted to lower energies, and therefore in better agreement with the experimental data. Finally the TOF spectra simulated from the AIMD reaction probability curves agree better with experiment than the ones simulated using the BOSS reaction probability curves.

This chapter is structured as follows. In Sections 4.2.1-4.2.3 we describe the theoretical methods employed (BOSS model, AIMD methods and hole model). In Section 4.2.4 the various functional forms which have been used in the fitting of the reaction probability curves are presented. In Sections 4.2.5-4.2.7 we describe how the experimental state-selected reaction probability curves have been extracted from the measured TOF spectra and how the relative and absolute saturation values of these curves have been determined. In Section 4.2.8 we show how the average desorption energy can be computed from the state-selected reaction probability curves. In Section 4.3, all the results are presented and discussed: Section 4.3.1 includes the hole model results; in Section 4.3.2 all the fits of the theoretical reaction probabilities are presented; in Sections 4.3.3 and 4.3.4 the fits of the experimental TOF spectra, and the reaction probabilities extracted from these are presented, respectively; in Section 4.3.5 simulated TOF spectra are presented and compared to measured ones; in Sections 4.3.6 and 4.3.7 the effective barrier heights and average desorption energies obtained theoretically and experimentally are compared. Finally, conclusions are presented in Section 4.4.

4.2 Methods

4.2.1 BOSS Model

Details about the BOSS model are given elsewhere [39,40], therefore only a brief description is given here. An accurate six-dimensional potential energy surface (PES) [39, 40], based on a large number of DFT calculations, describes the interaction between H_2 and

the ideal Cu(111) surface. The semi-empirical SRP functional [39] was employed in the electronic structure calculations. The SRP-PES is characterized by a minimum barrier height (E_b) of 0.628 eV, which corresponds to the so-called bridge-to-hollow (bth) configuration [39]. For D_2, zero-point energy (ZPE) corrections lower the barrier by about 30 meV. Further barrier heights with the relative barrier geometries can be found in Table 4.A.1. We report calculations performed using the quasi-classical trajectory (QCT) method, the appropriateness of which is justified by the good agreement between quantum and quasi-classical dynamics results found previously [39, 40]. In the QCT method, vibrational ZPE is imparted to the molecule, the initial conditions of which are described via an appropriate sampling of coordinates and velocities.

4.2.2 AIMD Method

The AIMD technique [72,73] relies on the Born-Oppenheimer approximation, as does the just described BOSS model. However, due to the 'on-the-fly' calculation of the forces, AIMD circumvents the need of computing and fitting a PES and allows for the simulation of surface atom motion, which is used to model the experimental surface temperature (T_s = 925 K [13]). The procedure according to which the initial displacements from the equilibrium positions and the velocities are assigned to surface atoms is described in Ref. [43] and Chapter 3. Note that the equilibrium lattice constant has been expanded by 1.54% [74,75] in order to account for thermal expansion. Just like the BOSS calculations, the AIMD calculations use the QCT method. The AIMD technique has already been shown [43] to quantitatively reproduce the sticking probability measured by Michelsen et al. [13] using molecular beam experiments (see Figure 3.1 in Chapter 3).

The AIMD calculations are performed with the VASP package [76–80]. The surface is modeled using a slab consisting of 4 layers, three of which are allowed to move. A 2x2 supercell is employed. The first Brillouin zone is sampled by a 8x8x1 k-point grid which includes the Γ point. Other computational details, which are given elsewhere (Ref. [43] and Chapter 3), are very similar to the ones used in the BOSS calculations. The SRP48 functional used here differs from the original SRP functional [39] in the use of the PBE

exchange-correlation functional [81, 82] instead of the PW91 one [83, 84], and in the use of a slightly different mixing coefficient (see Ref. [43] and Chapter 3 for more details). However, with the mixing coefficient chosen, the SRP48 functional reproduces the SRP minimum barrier height [43]. Calculations suggest that surface temperature should have little effect on the barrier heights that would be extracted from dynamics experiments. If only thermal expansion of the surface is considered, the barrier heights computed for high symmetry sites are significantly lowered (by 27 to 44 meV at T_s = 925 K) [85], provoking a shift of the reaction probability curves towards a lower energy [44, 85]. Dynamics calculations suggest that this effect is counteracted by the displacement of surface atoms from their equilibrium position [44] and from the modeling of dynamical recoil effects [43], which tend to shift the reaction probability curve by the same amount of energy, but in the opposite direction. The net effect observed in the calculations is a broadening of the reaction probability curve, though not by the same amount as observed experimentally.

Between 400 and 900 trajectories per initial rovibrational state and collision energy have been computed. Reaction probabilities and confidence intervals are estimated with the Wilson (or score) [86] method, except if a zero binomial proportion is observed (if no reactive events are found), for which case a proper interval has been employed [87]. Reaction probability error bars represent 68.3% confidence intervals.

4.2.3 The Hole Model

The consequence of the multidimensionality of the PES for an activated system like H_2 + Cu(111) is that each molecule experiences a different energy barrier along the path it attempts to follow towards reaction. Formally, the barrier distribution function $N(E)$ is the fractional number of barriers with an energy which falls between E and $E + dE$. According to the classical hole model [66, 67] the reaction probability S as a function of the collision energy E_i can be computed from the barrier distribution function:

$$S(E_i) = \int_0^{E_i} N(E')dE'. \tag{4.1}$$

This model assumes the applicability of a sudden model to the parallel translational motion and the rotation of the molecule, and a purely classical over-the-barrier mechanism: no effects such as tunneling or vibrational softening at the transition state are considered. The model also assumes that the only energy available for the reaction is the collision energy. Note that $N(E)$ is determined from a (static) analysis of the PES, therefore $S(E)$ cannot be initial-state specific. We expect this model to be reasonable for $(v = 0, J = 0)$ H_2, which contains only zero-point vibrational energy, and for which each orientation is equally likely. Dai and Light [35] have shown that for this state, and for the translational energies of interest to our study, the reaction probability can be accurately computed by summing fixed-site reaction probabilities with appropriate weights, meaning that the sudden approximation may be assumed to work reasonably well at least for parallel translational motion. The analysis with the hole model, which involves the evaluation of $N(E)$ from the PES and the calculation of $S(E)$ according to Equation 4.1, is likely to demonstrate whether it is likely that an asymmetric fitting function should be employed to fit the sticking probability for at least the $(v = 0, J = 0)$ state. Fitting TOF spectra for other (v, J) states with a fitting function that is flexible enough to both describe asymmetric and symmetric sticking probability curves can then show to what extent the results of the hole model regarding asymmetry of the reaction probability curve generalize to other (v, J) states.

$N(E)$ is often arbitrarily assumed to be a Gaussian function [88]. With this assumption, we can rewrite Equation 4.1 as [88]:

$$S(E) = \frac{A}{\sqrt{\pi}W} \int_0^E \exp\left[-\left(\frac{E' - E_0}{W}\right)^2\right] dE' = \frac{A}{2}\left[1 + \mathrm{erf}\left(\frac{E - E_0}{W}\right)\right]. \qquad (4.2)$$

This result motivated the use of a form (ERF) incorporating the error function to model the reaction probability curve for activated systems [89, 90]. For instance, the reaction probability of the systems H_2+Cu(111) [16], D_2+Cu(111) [13], N_2+W(110) [68], CH_4+Pt(111) [69], CH_4+Ni(111) [70] and H_2O+Ni(111) [71] has been modeled with the ERF form. More generally, any $N(E)$ symmetric about E_0 will give a $S(E)$ that is symmetric with respect to inversion about its inflection point, for which $E = E_0$.

However, application of the hole model to a non-symmetric barrier distribution function would lead to a reaction probability curve that is 'non-symmetric' with respect to the inflection point. Such a curve would not be properly described by the ERF functional form.

The ERF form (Equation 4.2) is symmetric with respect to inversion through its inflection point, increases monotonically and has an upper asymptote at $S = A$. In the literature, people often refer to A, E_0 and W as the saturation parameter, the effective barrier height and the width parameter respectively.

In order to test the degree to which the barrier distribution function $N(E)$ for H_2 + Cu(111) resembles a Gaussian distribution, we have calculated $N(E)$ from the accurate six-dimensional PES [39, 40] by computing the energy distribution of the first-order saddle points (transition states) found in more than 10^7 (r, Z) cuts of the PES, using a small bin width. A modified Newton-Raphson approach as described in Ref. [91] has been used to locate the transition states. The two-dimensional cuts were chosen on a grid in X, Y, cosθ and φ: X and Y uniformly cover the surface unit cell, and cosθ and φ uniformly range from -1 to 1 and from 0 to 2π, respectively. Note that $N(E)$ is normalized by the total volume of possible configurations.

4.2.4 Reaction Probability Curve Fitting

Previous work in fitting $S(E)$ to experimental dissociative adsorption and associative desorption measurements have used either the ERF or the hyperbolic tangent (TANH) functions. Both are symmetric with respect to inversion about their inflection points [7, 92]. As we will see in Section 4.3.1, the hole model predicts an asymmetric barrier distribution, $N(E)$. We are thus motivated to try sigmoidal fitting functions that are flexible enough to allow for $S(E)$ curves that are not symmetric with respect to inversion about their inflection point. Figure 4.2 displays the asymmetric functions we have tried in comparison to the ERF and TANH functions.

One of these is the generalized logistic function (LGS):

$$S(E) = \frac{A}{\left[1 + \nu \cdot \exp\left(-\frac{E-E_0'}{W'}\right)\right]^{\frac{1}{\nu}}}. \tag{4.3}$$

The $\nu = 1$ special case of the LGS function is the ordinary logistic curve, a function which is symmetric with respect to inversion through its inflection point and can be related to the TANH function:

$$S(E) = \frac{A}{1 + \exp\left(-\frac{E-E_0'}{W'}\right)} = \frac{A}{2} \cdot \left[1 + \tanh\left(\frac{E - E_0'}{2W'}\right)\right]. \tag{4.4}$$

Another special case of the LGS function is obtained for $\nu \to 0^+$; this limit corresponds to the Gompertz function (GMP), a sigmoid curve which approaches the upper asymptote more gradually than the lower one (and is therefore 'non-symmetric' with respect to the inflection point):

$$S(E) = A \cdot \exp\left[-\exp\left(-\frac{E - E_0'}{W'}\right)\right]. \tag{4.5}$$

Note that for the LGS function the value of W' itself is not strictly related to the 'broadening' of the curve; the width of the curve also depends on the value of ν. This is illustrated by Figure 4.2B, which includes curves with different values of ν but the same W' and E_0' value: all the curves have similar widths above the inflection point, but the TANH curve is significantly broader than the GMP curve below the inflection point. The broadening of the different curves can be compared through a parameter defining the broadening of a curve in an absolute sense. We define the parameter W with the same physical meaning as the width parameter of the ERF form, i.e. half of the additional collision energy necessary to raise the reaction probability from $S(E_0 - W)$ to $S(E_0 + W)$:

$$W = \frac{1}{2} \cdot \left[S^{-1}\left(\frac{A}{2}\left[1 + \mathrm{erf}(1)\right]\right) - S^{-1}\left(\frac{A}{2}\left[1 + \mathrm{erf}(-1)\right]\right)\right]. \tag{4.6}$$

Additionally, W_1 and W_2 are defined as the parameters that allow us to distinguish

between the broadening of the low energy portion and the high energy portion:

$$W_1 = E_0' - S^{-1}\left(\frac{A}{2}\left[1+\mathrm{erf}(-1)\right]\right), \tag{4.7a}$$

$$W_2 = S^{-1}\left(\frac{A}{2}\left[1+\mathrm{erf}(1)\right]\right) - E_0'. \tag{4.7b}$$

A function with a larger number of parameters, which is therefore more flexible, arises from the product of the GMP and the TANH. We refer to this function, which contains five parameters, as the five parameter curve (FPC):

$$S(E) = A \cdot \frac{\exp\left[-\exp\left(-\frac{E-E_0'}{W'}\right)\right]}{1+\exp\left(-\frac{E-E_0''}{W''}\right)}. \tag{4.8}$$

The values that a specific parameter assumes if the same functional form is fitted to various sets of data can give indications about general trends. However, we use parameters with a physical meaning for comparisons independent on the functional form employed in the fitting. For all the investigated functions, we define the effective barrier height E_0 using the physical meaning that this parameter has for the ERF form (Equation 4.2), i.e. the energy at which the reaction probability first reaches half the saturation value of the reaction probability curve: $E_0 = S^{-1}(A/2)$. Note that according to the current definition of E_0, the effective barrier height for a certain initial state is the energy larger than 50% of the dynamical barriers, i.e. the median of the dynamical barrier distribution. The dynamical barrier distribution can differ significantly from the barrier distribution function $N(E)$ described in Section 4.2.3, since the former also includes dynamical effects that are specific for each rovibrational state while the latter is a 'static' property of the PES. In a similar way, E_0, the effective barrier height, has a different meaning from E_b, the static minimum energy barrier: the former is the median of the dynamical barrier distribution, while the latter is the minimum energy required to react on a specific PES within a classical approximation, and represents the onset of the barrier distribution function $N(E)$.

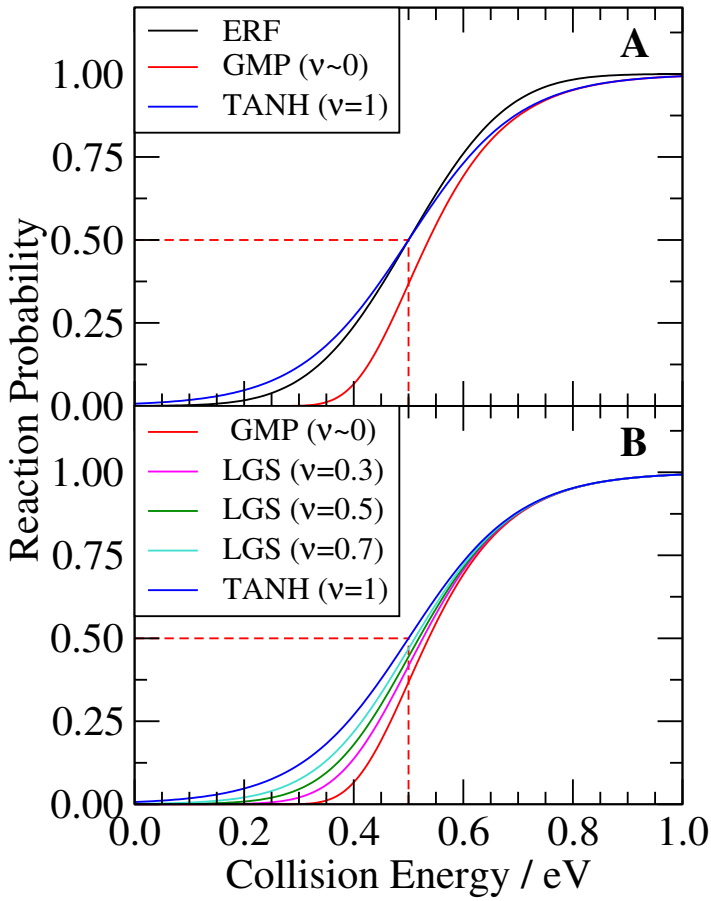

Figure 4.2: Illustrative representation of the various functions used to model the reaction probability curves. (A): the error function (ERF, black, $E_0 = 0.5$ eV, $A = 1$, $W = 0.2$ eV) is compared to the two limiting cases of the logistic function ($E_0' = 0.5$ eV, $A = 1$, $W' = 0.1$ eV), which are the hyperbolic tangent (TANH, blue, obtained for $\nu = 1$) and the Gompertz function (GMP, red, obtained for $\nu \to 0^+$). (B): the same TANH and GMP functions as in panel A are plotted together with logistic functions obtained with $E_0' = 0.5$ eV, $A = 1$, $W' = 0.1$ eV and intermediate values of ν.

4.2.5 Time of Flight (TOF) Spectra Analysis

In the present work, we perform a re-analysis of the raw data from Ref. [13] (a description of the experimental apparatus can be found there). D_2 molecules desorbing from a single crystal surface were detected via laser ionization. The experimental conditions were such that the flight time t' of the ions from the laser to the detector was dominated by the flight time t in a field-free region.

According to the principle of detailed balance, the recorded TOF spectra can be related to the initial-state-selected reaction probabilities. In particular, the TOF intensity at the field-free flight time t is given by a flux-weighted velocity distribution (expressed in the time domain) multiplied by the reaction probability S and divided by the velocity $v = x/t$, to account for the fact that the detection method used (REMPI) yields a signal that is proportional to the density in the probe volume:

$$I\left(t,\theta,\varphi\right)\sin\theta d\theta d\varphi dt = K\cdot\exp\left(-\frac{m(x/t)^2}{2k_bT_s}\right)\left(\frac{x}{t}\right)^4 S\left(E_n\right)\cos^2\theta\sin\theta d\theta d\varphi dt. \quad (4.9)$$

Here K is a proportionality constant, m is the mass of the D_2 molecule, k_b is the Boltzmann constant, T_s is the surface temperature, θ and φ identify the polar and the azimuthal desorption angles, respectively, and x is the distance flown by the molecules in the field-free region. We assume normal energy scaling, therefore $S = S(E_n)$, E_n being the energy associated with motion of the molecules normal to the surface: $E_n = mv^2\cos^2\theta/2$. Equation 4.9 is slightly different from the TOF intensity expression originally used (Equation 4.2 of Ref. [13]). Here we take into account that molecules traveling along a linear path that makes an angle θ with the surface normal have flight lengths x that depend on θ, i.e. $x = L/\cos\theta$, where L is the length of the field-free region. In contrast, $x = L$ was originally assumed; in Equation 4.9 the $\cos^2\theta$ factor, in place of the originally used $\cos\theta$, also comes from the variation in x with θ.

The experimental apparatus, schematically represented in Figure 4.3, dictated some geometrical constraints on the desorbed molecules reaching the detector and contributing to the signal. We can assume that the laser was focused along a short line, whose length

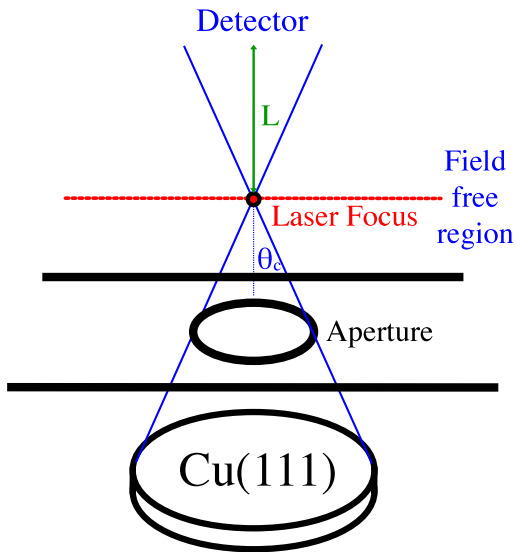

Figure 4.3: Schematic representation of the experimental apparatus.

was determined by the laser optics. In the limit of a point detector, only the molecules in a cone with the crystal as base and the crystal-detector distance as height were ionized. To account for this, we have to integrate Equation 4.9 over a solid angle with the same aperture as the cone just described, estimated to be approximately 40° from the experimental setup. This integration is performed over the azimuthal and the polar coordinates φ and θ, from 0 to 2π and from 0 to θ_c, respectively, θ_c being half the aperture of the cone ($\theta_c = 20°$). We also analyzed some representative TOF spectra assuming that the detector is focused to a line segment parallel to the surface. Under this assumption, the molecules contributing to the signal were the ones for which a straight path from the surface to the line segment and through the aperture located between them was available. However, results obtained assuming a line detector with length up to 9.4 mm are not considerably different from the ones obtained under the assumption of a point detector (fitted E_0' and W' values differ by less than 15 meV). For this reason, we have considered the point detector approximation as valid for the rest of the analysis.

The observed total flight time t' has to be corrected [13] by subtracting from it $t_{corr} = 1.79$ μs, which is the time the ions flew after leaving the field-free region, in order to obtain the field-free flight time t. The low energy ions were deflected more

easily than the high energy ones, resulting in a distortion of the spectra which can be reproduced by multiplying Equation 4.9 by the following 'cut-off' function [13]: $f(t') = 1 - \tanh\left[\left(t' - t_c\right)/t_w\right]$, with $t_c = 19.5$ μs and $t_w = 6.6$ μs. The final expression obtained for the TOF signal at the observed time t' corresponding to the field-free flight time t is the following:

$$I\left(t'\right)dt' = K' \int_{\varphi=0}^{2\pi} d\varphi \int_{\theta=0}^{\theta_c} I\left(t,\theta,\varphi\right) \sin\theta d\theta \left[1 - \tanh\left(\frac{t' - t_c}{t_w}\right)\right] dt'. \tag{4.10}$$

Here $t' = t + t_{corr}$. The calibration procedure, which was originally performed without angular averaging, has been repeated using the new expression of the TOF intensity (which includes the integration over the solid angle). This calibration returned a length L of the field-free region of 23.7 mm, as compared to the earlier estimated value of 24 mm.

Equation 4.10 has been fitted to experimental TOF spectra in order to extract the D_2 reaction probabilities $S(E_n)$ (note that the dependence on $S(E_n)$ is in the term $I(t,\theta,\varphi)$, see also Equation 4.9). Note that a thermal (300 K) background has been subtracted from some of the measured spectra [13]. The Levenberg-Marquardt algorithm [93,94], as implemented in the MINPACK library [95,96], has been employed in order to minimize the sum of the squared residuals. Spectra have been fitted over the range of times for which the signal is $\geq 5\%$ of the maximum signal. The goodness of the fits has been evaluated on the basis of the value of χ^2, the sum of the squared residuals. Error bars in the fitted parameters represent 68.3% confidence intervals and have been estimated from replicate measurements.

For further analysis, we have also extracted reaction probabilities directly from the TOF spectra, using the following expression:

$$S\left(E_n\right) = \frac{K \cdot I\left(t'\right)dt'}{\int_{\theta=0}^{\theta_c} \exp\left(-\frac{m(x/t)^2}{2k_b T_s}\right)\left(\frac{x}{t}\right)^4 \cos^2\theta \sin\theta d\theta dt'}. \tag{4.11}$$

In practice, the TOF intensity is divided by a 'θ-averaged' velocity distribution. Equation 4.11 is therefore valid only if normal energy scaling is assumed, under which con-

dition $S(E_n)$ is not a function of the θ angle and can be extracted from the integral in Equation 4.10. The comparison between fitted reaction probability curves and curves extracted from the TOF spectra using Equation 4.11 is a test of the ability of modeling $S(E_n)$ using the functional form employed in the fits.

Note that only the shape of $S(E_n)$ can be extracted from the fits of the absolute TOF spectra intensities, as no information about the saturation values (relative or absolute) of the reaction probability curves is contained in the absolute TOF signal by itself. To determine relative saturation values, it is necessary to compare the desorption intensities to intensities recorded from a Knudsen source. Absolute saturation values can only be obtained by comparing the fitted curves to adsorption data.

4.2.6 Determination of the Relative Saturation Values

In order to determine the relative saturation values of the various reaction probability curves we have to compare the vibrational populations computed from the initial-state-selected reaction probabilities, assuming unit saturation values, with the measured vibrational populations [13]. The latter can be determined by comparing the measured state-selected signals (integrated TOF intensities) to the intensities recorded from a Knudsen source. The former are computed by summing the rotational state populations corresponding to the same vibrational level; the rotational state population can be related to the initial-state-selected reaction probability $S_{v,J}$ in the following way [13]:

$$P(v,J) \propto F_{v,J}\left(T_s\right) \int_{E=0}^{\infty} dE \int_{\theta=0}^{\theta_c} \sqrt{E} \exp\left(-\frac{E}{k_b T_s}\right) S_{v,J}\left(E_n\right) \cos\theta \sin\theta d\theta, \qquad (4.12)$$

where $F_{v,J} = N \cdot (2J+1) \cdot d_{o-p}^{J} \cdot \exp\left(-\frac{E(v,J)}{k_b T_s}\right)$ is the Boltzmann factor corresponding to the (v,J) state, in which $E(v,J)$ is the internal energy of the state, N is a normalization constant and d_{o-p}^{J} is a factor which accounts for the ortho-para population ratio of D_2.

4.2.7 Determination of absolute saturation values

The sticking probabilities, which were measured directly by adsorption of molecules incident on the surface from a seeded supersonic molecular beam source, can be related to the initial-state-selected reaction probabilities determined by the application of detailed balance to desorption data through the following equation [11, 13]:

$$S_0\left(v_s, \alpha, T_n, \Theta\right) = \sum_{v,J} F_{v,J}\left(T_n\right) \int_{E=0}^{\infty} S_{v,J}\left(E_n\right) f\left(v_s, \alpha, E\right) dE + S_{atoms}. \tag{4.13}$$

Here T_n is the nozzle temperature, S_{atoms} is the contribution to the sticking probability from D atoms in the beam (estimated from the stagnation pressure and nozzle temperature, assuming unity sticking probability for the atoms [11]) and $f(v_s, \alpha, E)$ is the velocity distribution of the molecules in the beam, characterized by the experimentalists and expressed as a function of the stream velocity (v_s) and a width parameter (α) [7].

In order to determine the absolute saturation values of the reaction probability curves obtained from the desorption experiments, Equation 4.13 has been least-squares fitted to adsorption data [11]. The relative saturation values among states have been kept fixed. Because the sticking probability values range over different orders of magnitude, we have performed the fit in two stages. First, the function $R_{\log} = \log(S_0^{exp}) - \log(S_0^{fit})$ has been employed as residual function. In order to account for the different surface temperature between adsorption and desorption experiments, the absolute values of the width parameters W' characterizing the initial-state-selected reaction curves were allowed to vary, but the relative values of W' were constrained to the ratios determined from the desorption data. In the second stage of the fit, in order to make the fit more sensitive to the saturation values, another residual function has been minimized, keeping the W' parameters (and therefore the 'shape') of the reaction probability curves fixed to the values determined in the first stage: $R = S_0^{exp} - S_0^{fit}$.

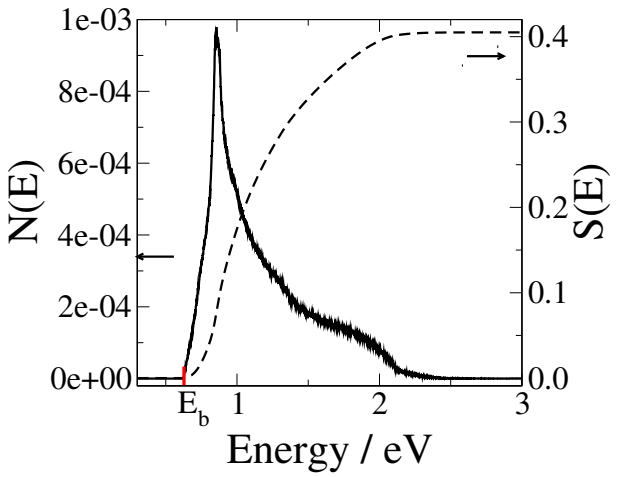

Figure 4.4: Barrier distribution function $N(E)$ computed from the PES of Ref. [39, 40] (solid line) and sticking probability $S(E)$ evaluated according to the hole model (dashed line). Note that the minimum energy barrier ($E_b = 0.628$ eV) has been marked in red on the energy axis.

4.2.8 Average Desorption Energy

The average desorption energy has been computed from the initial-state-selected reaction probabilities using the following expression [7]:

$$\langle E_{trans} \rangle = \frac{\sum_{v,J} F_{v,J}\left(T_s\right) \int_{E=0}^{\infty} E^2 \exp\left(-\frac{E}{T_s}\right) S_{v,J}\left(E_n\right) dE}{\sum_{v,J} F_{v,J}\left(T_s\right) \int_{E=0}^{\infty} E \exp\left(-\frac{E}{T_s}\right) S_{v,J}\left(E_n\right) dE}. \tag{4.14}$$

4.3 Results and Discussion

4.3.1 Hole Model Results

The barrier distribution function $N(E)$ computed from the SRP-DFT PES is plotted in Figure 4.4. Note that the onset of $N(E)$ is, as expected, at $E_b = 0.628$ eV, the minimum energy barrier in the PES. The distribution presents a broad high-energy tail and is therefore non-symmetric. Consequently, the sticking probability $S(E)$ estimated according to the hole model (Figure 4.4) is also non-symmetric and would not be expected to be fitted accurately by the ERF expression.

4.3.2 Fits to BOSS and AIMD Reaction Probabilities

BOSS initial-state-selected reaction probabilities, computed from the same PES for which the barrier distribution has been evaluated, have been fitted using the ERF, the LGS and the FPC expression. Results of the fitting for some representative initial states are shown in Figure 4.A.1. Table 4.A.2 contains the parameters obtained from these fits. The best fits (as based on χ^2 values) are obtained using the flexible FPC expression, since it contains the largest number of parameters (see Table 4.A.2). The LGS generally produces good quality fits. We observe a ν parameter which is close to zero for all the examined states, which means that the non-symmetric (GMP) form of the LGS expression better fits the BOSS data than the symmetric (TANH) limit of the LGS form. Note that both the FPC expression and the LGS expressions perform better than the ERF expression in fitting the data. The fact that non-symmetric functions effectively produce better fits of the BOSS reaction probabilities, in addition to the shape of the barrier distribution function calculated from the PES, suggests that non-symmetric functions might in general yield a better description of experimental reaction probabilities as well.

AIMD initial-state-selected reaction probabilities have also been fitted using both the ERF and the LGS expressions. Fitted curves are plotted in Figure 4.A.2, and the corresponding parameters are included in Table 4.A.3. Due to the higher computational cost of AIMD, we were able to investigate fewer collision energies (5) than what has been done with the BOSS model (20). As a consequence, the scatter is larger and we observe larger variability in the shape of the fitting functions across states. For the $(v = 0, J = 4)$ initial state, we investigated one additional collision energy compared to the other initial states. The ERF and LGS fits of the 5 lower collision energy points for this initial state were almost superimposed (see dashed lines in Figure 4.A.2, $(v = 0, J = 4)$). In order to check whether this result was a statistical fluke, we included a sixth high collision energy to the set of data. The inclusion of this collision energy confirmed that this was indeed the case, since the LGS and ERF fits are now considerably different. Considering all the investigated initial states, the LGS form produces better fits than the ERF form for

the AIMD data, as is the case for the BOSS results. Due to the lower number of AIMD reaction probability points compared to the BOSS results, we consider the AIMD results reliable only in the range of collision energies for which we have data. Having said that, the LGS fits of the AIMD reaction probabilities look somewhat broader than the LGS fits of the BOSS data (see Figure 4.5). The AIMD reaction probabilities are generally larger than the BOSS ones close to the threshold. The noise in the AIMD fits can be reduced by removing one fitted parameter; for instance, we can constrain the saturation values of the AIMD fits to the corresponding values from the BOSS fits. In most cases the AIMD curves remain slightly broader than the BOSS ones (except for $v = 0, J = 4$) and are slightly shifted to lower energies (see Figure 4.A.3), which is consistent with observed effects of surface temperature [21, 44]. However, the broadening observed when going from the BOSS (ideal, frozen lattice) to the AIMD ($T_s = 925$ K) reaction probability curves, is much smaller than the broadening observed experimentally [21].

4.3.3 Fits of measured TOF spectra

The measured TOF spectra have been fitted modeling the reaction probability curves with the ERF and the LGS expressions. Better fits of the experimental spectra are obtained if the LGS is employed, even though reasonable fits are obtained using both functions (see Figure 4.6, and Table 4.A.4 for the corresponding fitting parameters). Especially for the $v = 0$ rotational states, lower χ^2 values are obtained with the LGS fits. We also tested the use of the FPC form in the fits, but this function turned out to pair lack of stability to its higher flexibility in some cases and to give results not considerably different from the LGS ones in other cases. The relative quality of the fits performed with the symmetric ERF expression increases with increasing vibrational quantum number v, but the LGS fits are better in all cases, even for $(v = 2, J = 2)$ where $\nu = 1.0$, meaning that the symmetric TANH expression is used (Equation 4.4).

The values of the E_0 parameter obtained from the ERF fits of the TOF spectra using Equation 4.10 are slightly larger than the values obtained previously. This is clearly visible in Figure 4.7, where the E_0 values from the new ERF fits are compared

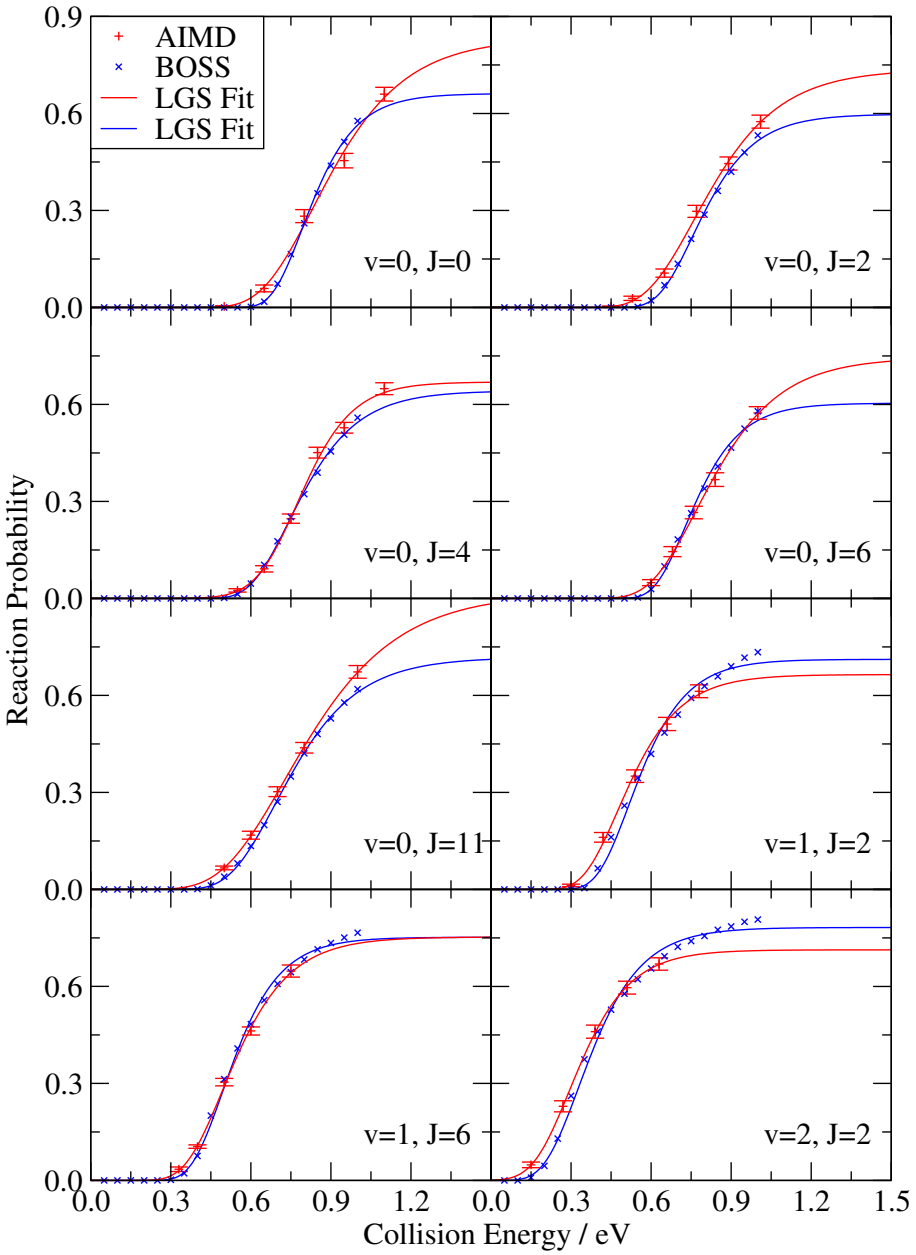

Figure 4.5: BOSS and AIMD reaction probabilities (blue × and red +, respectively) are plotted as a function of the collision energy for some representative initial states; the solid lines represent LGS fits of the probabilities.

to the earlier values [13]. This is due to the fact that our new TOF expression takes into account the longer flight paths of molecules traveling at non-zero angle from the surface normal. The fitted W parameters, on the other hand, do not change significantly if the new expression of the TOF signal is employed (see Figure 4.A.4). If the LGS is employed in the fits, the same trend in E_0' is observed as for the ERF form in E_0: E_0' first increases with J (up to $J = 4 - 5$) and then decreases (see Figure 4.A.5 A).

The shape of the fitted reaction probability curve depends on the vibrational state. The LGS form that fits the experimental data best is close to a GMP function (ν parameter close to 0) for low v but ν increases with v until the LGS form takes on the hyperbolic tangent form (a symmetric function, the LGS form with $\nu = 1$) for $v = 2$ (Figure 4.A.5 C). This suggests that dynamical effects lead molecules in high vibrational states to sample a distribution of effective barrier heights which is more symmetric than the distribution which appears to govern the reaction of D_2 in the lowest vibrational state.

In order to compare the widths of the $v = 0, 1$ and 2 LGS curves, we also calculated the W,W_1 and W_2 parameters for the fitted curves (see Section 4.2.4, Equations 4.6, 4.7a and 4.7b respectively). The width parameter W computed for the $v = 0$ reaction probability curves is significantly larger than the values computed for $v = 1$ and $v = 2$, meaning that the $v = 0$ probability curves are broader than the $v = 1, 2$ curves (see Figure 4.A.6). In particular, the broadening of the high energy portion of the reaction probability curves differs substantially across states, while we observe that the LGS fits are very similar, independently from v, in the broadening of the low energy portion: in fact, W_1 does not vary much with v. The observation that the W_2 values are closer to the W_1 values for $v = 2$ than for $v = 0$ is consistent with the fit function being more symmetric for $v = 2$.

4.3.4 Experimental Reaction Probability Curves

Representative ERF and LGS reaction probability curves fitted to TOF spectra using Equation 4.10 are compared to the curves directly extracted from the TOF spectra us-

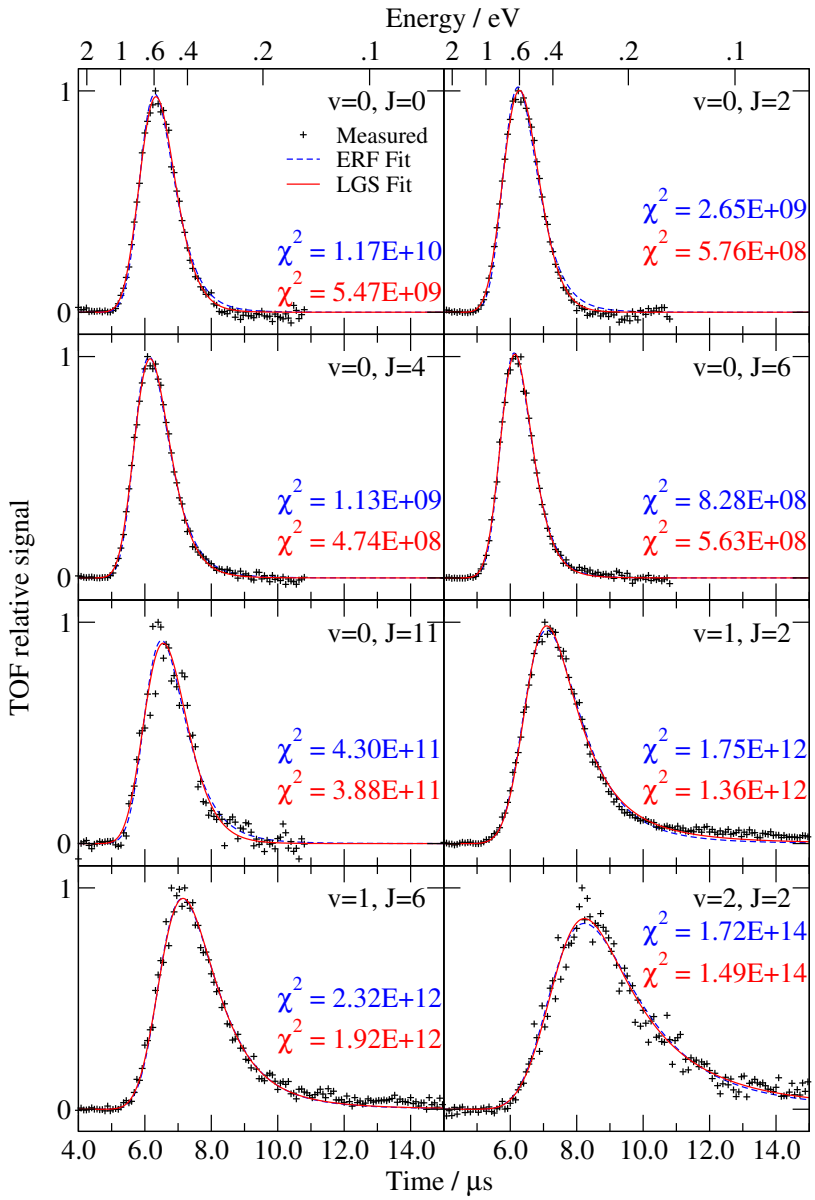

Figure 4.6: TOF intensities (black symbols) are plotted as a function of the detection time for some representative sets of data; dashed blue (solid red) lines correspond to TOF fits in which the ERF (LGS) form has been used to model the reaction probability curve. The sum of the squared residuals χ^2 is also reported for each fitted curve (in blue and red for ERF form and LGS form fit, respectively).

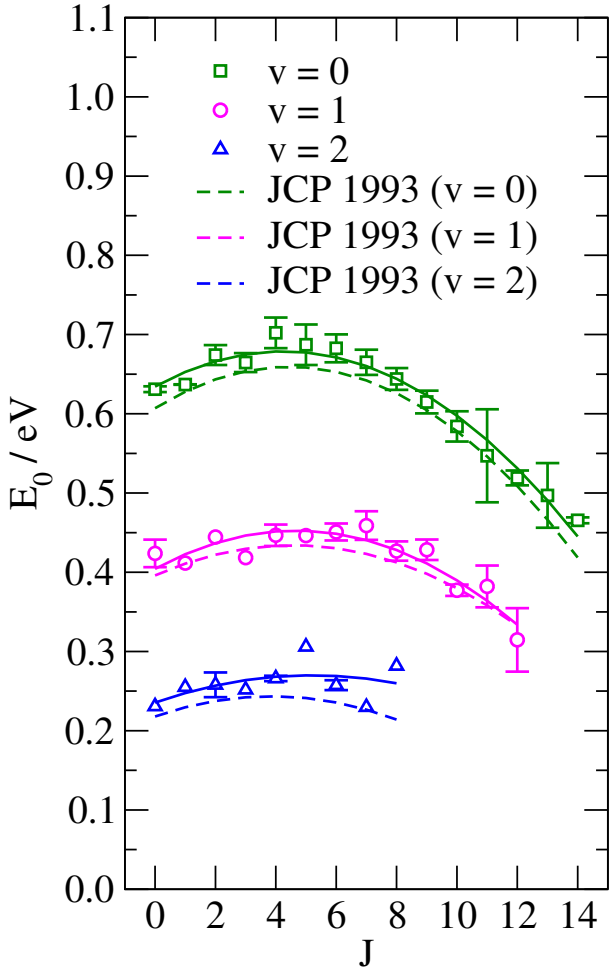

Figure 4.7: E_0 parameters obtained from ERF fits of all the available desorption TOF spectra are plotted as a function of the initial rotational state J. Green, violet and blue symbols correspond to $v = 0, 1$ and 2 initial vibrational states, respectively. Solid curves in the plot represent quadratic fits of the $v = 0, 1, 2$ data, while dashed lines are quadratic fits of the data using the method of Ref. [13]. Line colors are as for the symbols.

ing Equation 4.11 in Figure 4.8. Fitted ERF and LGS curves for the same state are in general very similar at low energies. However, the $v = 0$ LGS curves are characterized by saturation values significantly larger than the ERF ones. This is not the case for $v = 1$ and $v = 2$, where LGS and ERF fitted curves are quite similar over the whole energy range. Compared to the reaction probabilities directly extracted from the TOF spectra, the ERF fits generally underestimate the saturation values for $(v = 0, J)$ states, especially for the cases where the A values obtained with the LGS and ERF forms differ widely. Overall, the LGS seems to better describe the directly extracted reaction probabilities at high collision energies, even though it overestimates the reaction probability somewhat at high collision energies in a few cases ($v = 0, J = 2$ and $J = 6$ in the figure). The above observations are consistent with the finding that LGS fits of the experimental TOF spectra are clearly more accurate than ERF fits for $v = 0$, whereas the accuracy is more similar for $v = 1$ and $v = 2$ (see Figure 4.6). Given the fact that the main differences between ERF form and LGS form fits are observed at high energies, the transmission of the apparatus and the background subtraction procedure are unlikely to have influence on the fits. In fact, the transmission is close to one for most of the energies and small deviations are only expected at long times (low energies). Similarly, the subtraction of a thermal background might affect the reaction probabilities, but only at low energies, where the ERF and LGS forms are very similar [13].

The reaction probability curves obtained from the fits of the desorption data have been used to compute rotational populations via Equation 4.12, assuming a unit saturation value for all the curves. Next, vibrational populations have been computed by summing over the rotational populations corresponding to the same vibrational level. The ratio between the measured vibrational populations ($P(v = 1)/P(v = 0) = 0.25 \pm 0.07$ and $P(v = 2)/P(v = 0) = 0.015 \pm 0.004$) [13] and the ones computed in the just described way allows us to determine the relative saturation values of the initial-state-selected probability curves: $A(v = 0) : A(v = 1) : A(v = 2) = 0.96 : 1 : 0.81$. The relative saturation values are much closer to each other than the values previously obtained using ERF fits ($A(v = 0) : A(v = 1) : A(v = 2) = 0.54 : 1 : 0.77$) [13]. As in the

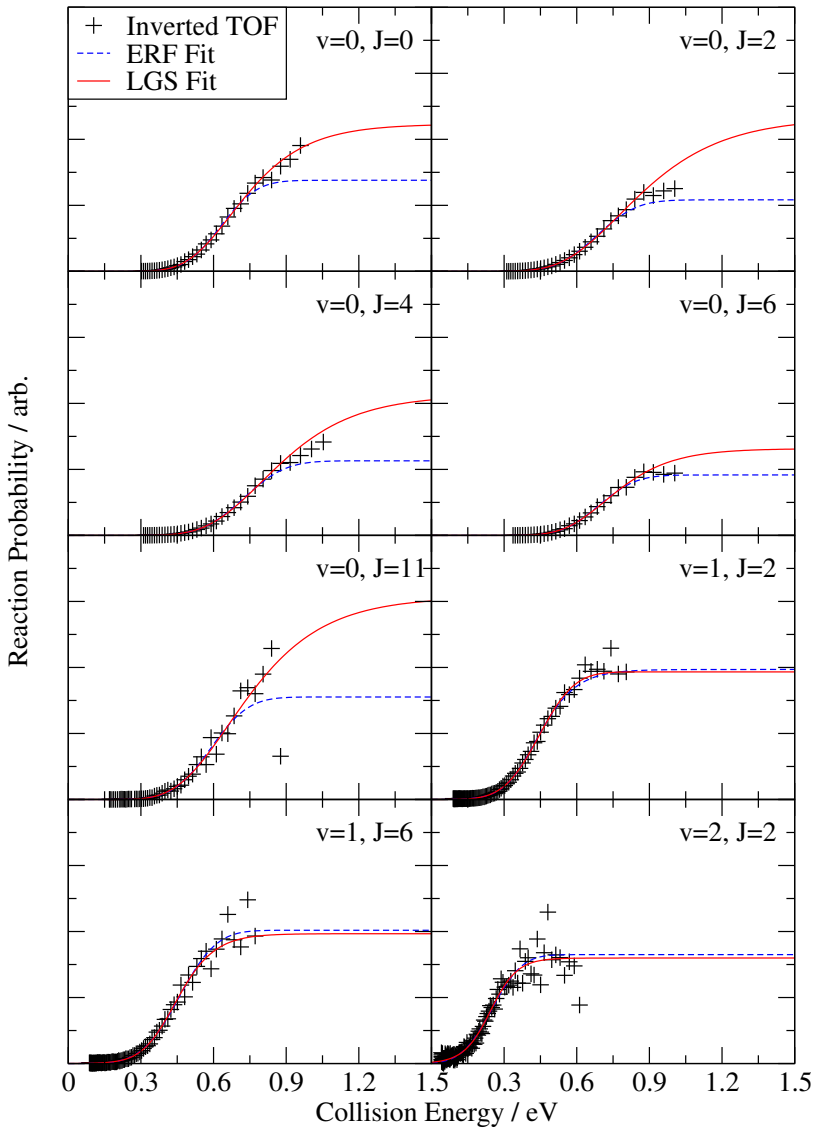

Figure 4.8: Reaction probability curves obtained from the fit of some representative TOF spectra are plotted as a function of the collision energy. Dashed blue (solid red) lines correspond to ERF (LGS) fits. Reaction probabilities directly extracted from the spectra are plotted as black symbols.

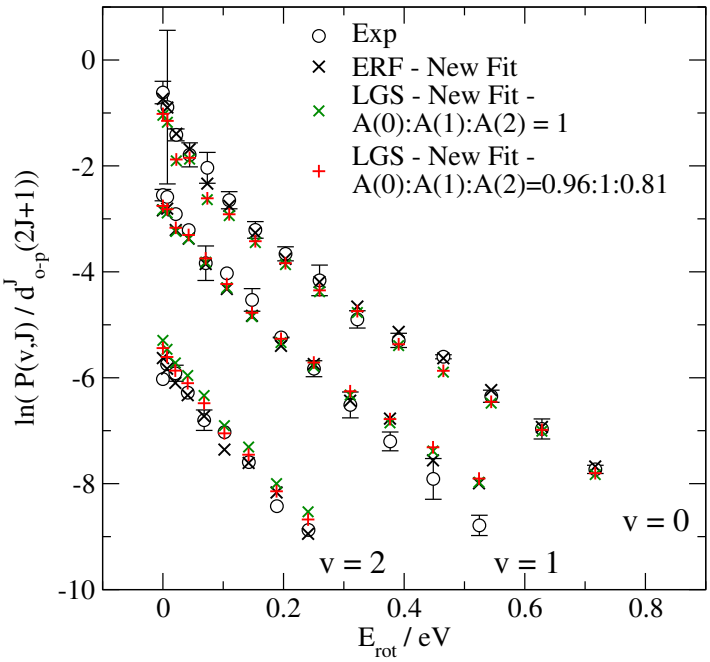

Figure 4.9: The measured rotational distribution (empty circles) is compared to the distribution computed from newly fitted reaction probability curves assuming the relative saturation values being 0.96:1:0.81 for $v = 0, 1$ and 2 (red +) and assuming the same saturation value across vibrational states (green $\times$). The rotational distribution computed from the newly fitted ERF-form reaction probability curves is plotted with black $\times$.

original analysis, we consider A to be independent of the rotational state: the measured rotational populations, plotted in Figure 4.9, are qualitatively reproduced under this assumption ($\chi^2 = 3.391$, close to the χ^2 value obtained using the original ERF fits: $\chi^2 = 3.193$). It is worth noting that even if the same saturation value is assumed for the three vibrational states ($A(v = 0) : A(v = 1) : A(v = 2) = 1 : 1 : 1$) we obtain population ratios that still agree with the measured populations within their error bars ($P(v = 1)/P(v = 0) = 0.239$ and $P(v = 2)/P(v = 0) = 0.0178$), and the rotational distribution remains reasonably well described ($\chi^2 = 4.197$, see Figure 4.9). Furthermore, the fact that similar saturation values are obtained for the different vibrational states is consistent with theory: the saturation values of the probability curves fitted to the BOSS and AIMD data do not differ considerably across states, if the same functional form is used (see Figures 4.A.1 and 4.A.2 and Tables 4.A.2 and 4.A.3).

Absolute saturation values of the reaction probability curves have been obtained by fitting the sticking probabilities obtained from adsorption experiments using the expression in Equation 4.13 while optimizing the A parameters and adjusting the W' parameters characterizing the initial state-selected reaction probability curves (see Section 4.2.7). The sticking probabilities measured with molecular beam experiments and the results of the fit are plotted in Figure 4.10. Overall, the sticking probability is reasonably well described using the LGS fitted curves. In particular, the sticking probability curve measured with seeded beams at the highest nozzle temperature (2100 K) is much better described in the high energy range than was achieved previously with the ERF fits, suggesting that our new A value for $v = 0$ is much more accurate than the old one (this is clearest if the measured sticking probabilities are plotted together with the fitted curves on a linear scale, see Figure 4.A.7). Absolute values of 0.47, 0.49 and 0.40 are obtained as saturation values for the $v = 0, 1$ and 2 probability curves, respectively, the earlier values being 0.27, 0.50, and 0.38 [15], respectively. The width parameters of the reaction probability curves obtained for the surface temperature at which the adsorption experiments were performed (120 K), are about 70% of the 925 K values. A similar decrease in the width parameter was observed in the original fits [13].

In Figure 4.11 the LGS reaction probability curves extracted from experiments are compared on an absolute scale to the theoretical results (BOSS model and AIMD). Overall, the theoretical curves are closer to experimental data in the onset of the reaction probability curves, compared to the previously fitted experimental curves (see also Figure 4.1). Furthermore, the experimental saturation values of the $v = 0$ probability curves (0.47) is significantly larger than the earlier value (0.27 [15]), resulting in better agreement with the theoretical results.

Unfortunately, the discrepancies between theory and experiment are not yet fully resolved: at high collision energies, theory still gives larger values for the reaction probability than does our reanalysis of the experimental raw data. Moreover, the effect that surface temperature has on the broadening of the reaction probability curves is much smaller for theory than for experiments: the AIMD ($T_s = 925$ K) curves are only slightly

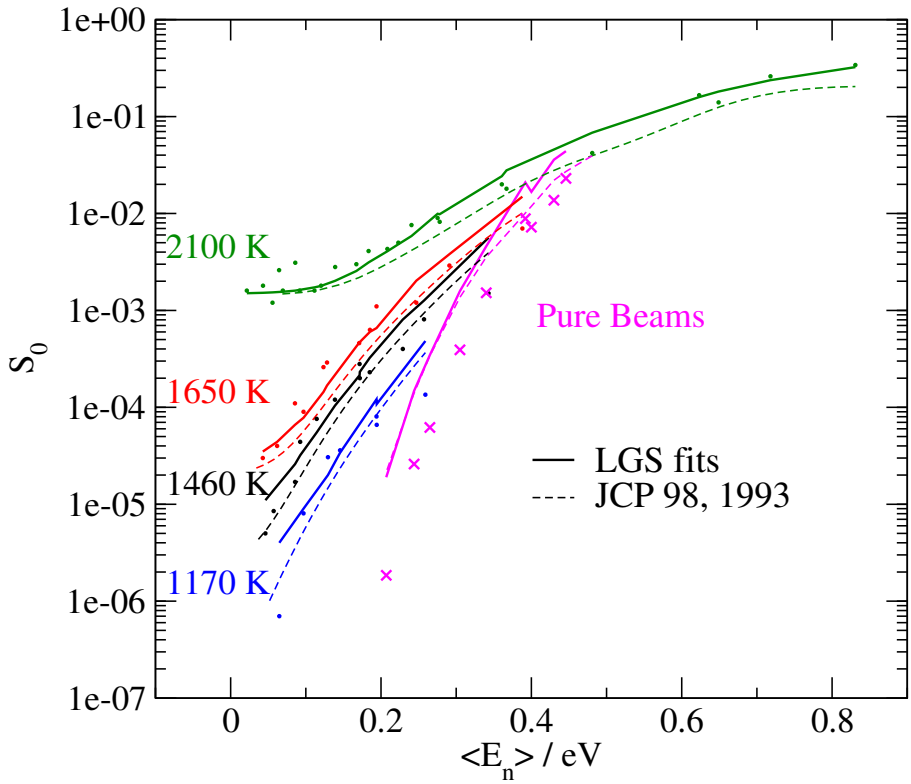

Figure 4.10: The sticking probability measured in molecular beam experiments is shown as a function of the average collision energy using a logarithmic scale. Seeded beam results corresponding to specific nozzle temperatures are plotted as circles, pure beam results using crosses. The results of our fits are plotted as solid lines. Dashed lines are from the previous fit (Ref. [13]).

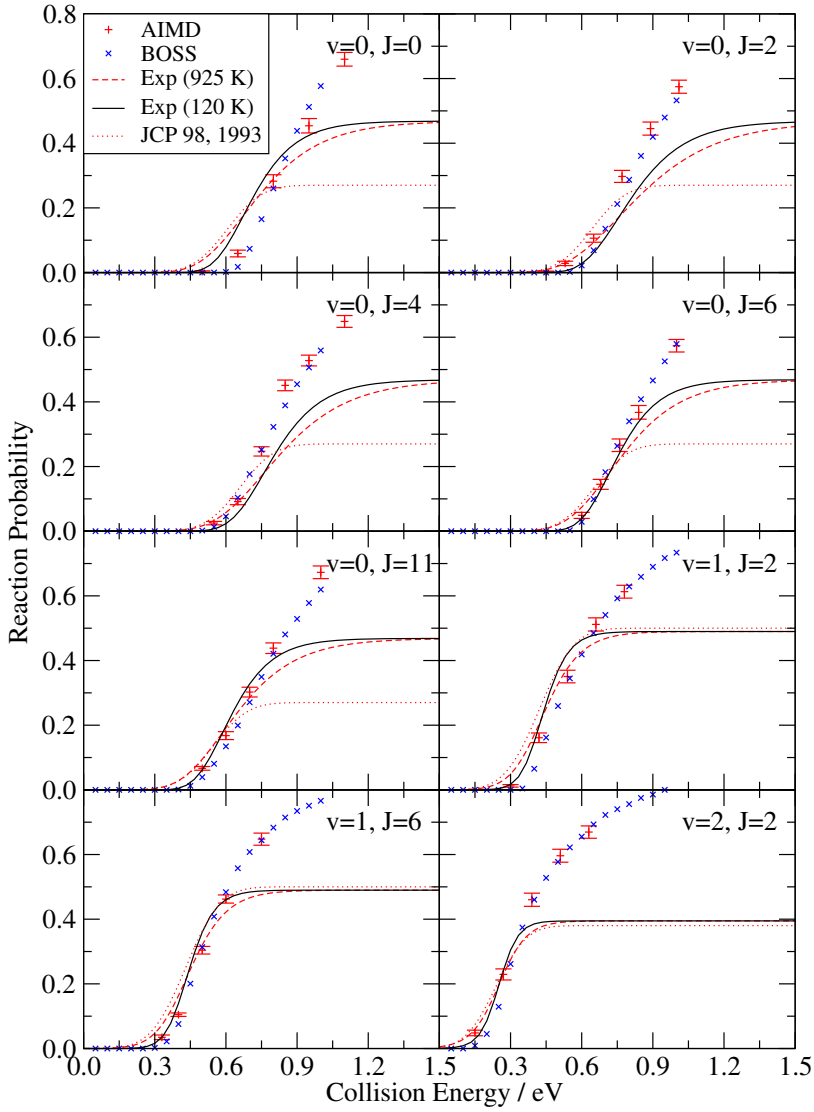

Figure 4.11: Experimental reaction probability curves for a surface temperature of 925 K (dashed red curve) and 120 K (solid black curve) are compared to theoretical data: BOSS (blue ×) and AIMD (red +). The reaction probability curves from Ref. [13] are plotted as red dotted curves for comparison.

broader than the BOSS ones (frozen ideal surface), in contrast with the large difference in width between the 120 K and 925 K experimental curves. The broadening we observe in theory is also much smaller than observed by Murphy and Hodgson, who studied the dependence of the reactivity on surface temperature [21]. The authors of this study also observed a surface temperature dependent low energy tail in the reaction probability curves which can not be described as a broadening effect. However, the AIMD method is not expected to be accurate at these collision energies, where S_0 is as low as 10^{-4}, given that a very large number of trajectories would be needed in order to provide statistically significant results (small error bars).

4.3.5 Simulated TOF Spectra

In Figure 4.12 A-C, TOF spectra simulated from the interpolated theoretical reaction probabilities are compared to experimental spectra for three representative states ($v = 0, 1, 2, J = 2$). The comparison between theory and experiment in the time domain highlights differences in the 'shape' of the reaction probability curves, without carrying any information on the saturation values. The theoretical spectra are generally too narrow compared to the experimental ones, and they peak at too short times. The AIMD spectra are broader than the BOSS ones, and therefore in closer agreement with experiments. Spectra much more similar to the experimental TOF are obtained from the theoretical models if the reaction probability curves are allowed to rigidly shift in energy (Figure 4.12 D-F, where the amount by which each reaction probability curve had to be shifted in order to best fit the corresponding experimental spectrum is presented is also reported). Note that the experimental TOF spectra are characterized by a sparser sampling of the high energies (short times) compared to the low energies (long times), as data have been measured at constant time intervals. Therefore, the fit of the theoretical data to the experimental spectra in the time domain is particularly sensitive to the low energy part of the reaction probability curves. In line with the better initial agreement with the experimental data, the shift required by AIMD to reproduce experimental data is smaller than for the BOSS model.

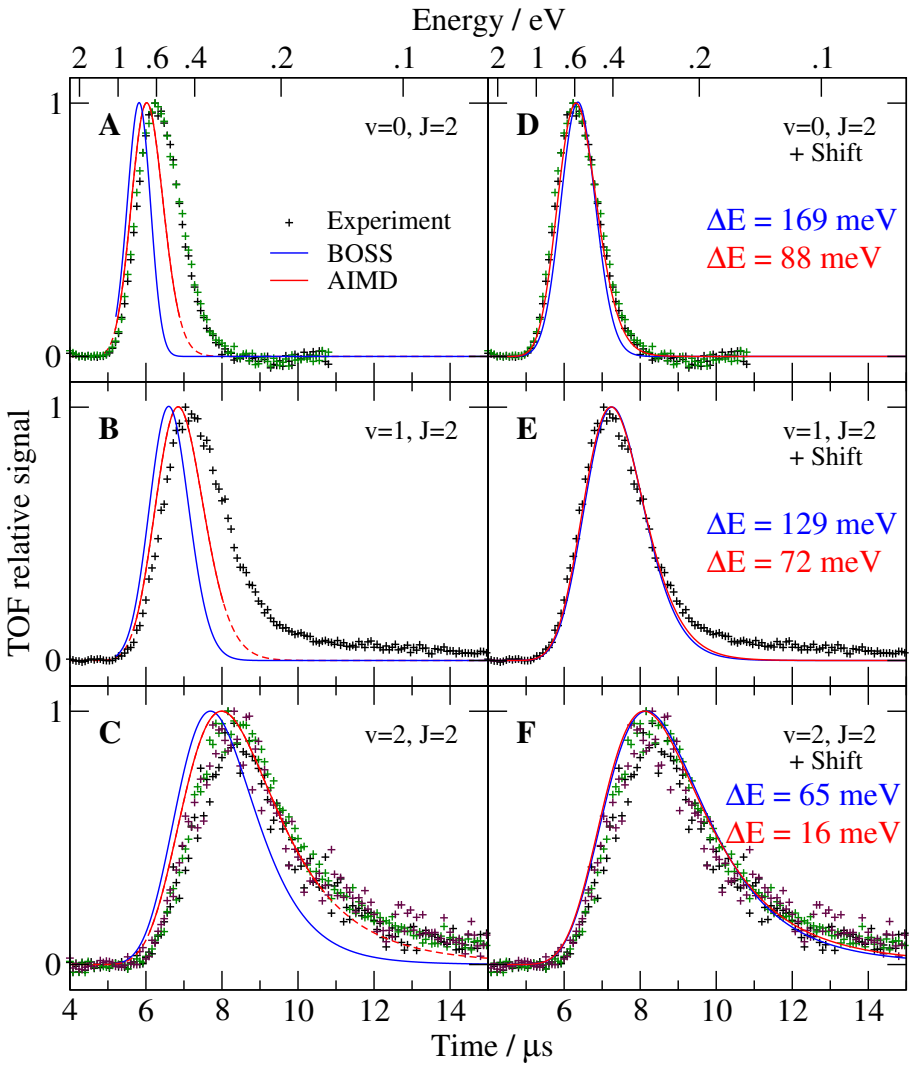

Figure 4.12: (A-C): TOF spectra calculated from theoretical reaction probabilities are plotted together with experimental data (symbols, different colors are used for different sets of measurements). Blue lines describe BOSS results, red lines AIMD results (solid lines indicate the time ranges which correspond to energies for which reaction probability points are available). (D-F): Simulated TOF spectra in which the reaction probability curves were free to shift along the energy axis in order to best fit the experimental data. The energy shifts ΔE (meV) applied to the theoretical reaction probability curves are reported (blue for BOSS and red for AIMD).

Model	Experiment	MAE (kcal/mol) (only $v = 0, 1$)	MAE (kcal/mol) ($v = 0, 1, 2$)
BOSS	Ref. [13]	1.482*	-
BOSS	New Fits	0.765	0.745
AIMD	New Fits	-	0.594

Table 4.1: Mean absolute error (MAE) computed for BOSS and AIMD values of E_0 with respect to the newly fitted experimental E_0. The value marked with (*) is from Ref. [39], where the BOSS results were compared to the previously fitted experimental data.

4.3.6 Experimental and Theoretical Effective Barrier Heights (E_0)

Another way of comparing theory with experiment is by plotting the E_0 value, defined as the collision energy at which the reaction probability equals half the saturation value of the corresponding experimental reaction probability curve. E_0 values extracted from experiments (note that E_0 differs from E_0' for the states characterized by a non-symmetric reaction probability curve), and from BOSS and AIMD calculations are plotted as a function of J in Figure 4.13. Table 4.1 contains the computed mean absolute error (MAE) for BOSS and AIMD, taking as a reference the quadratic fits of the experimental E_0. While single BOSS and AIMD E_0 values deviate from the experimental values by more than 1 kcal/mol, for both theoretical models the MAE is lower than 1 kcal/mol, the limit which defines chemical accuracy. The same level of accuracy is reached if the experimental points are chosen as the reference instead of their quadratic fits. The MAE obtained with the AIMD calculations is somewhat lower than obtained with the BOSS model. Chemical accuracy of the E_0 values could not yet be obtained for D_2 + Cu(111) using the earlier analysis [39, 40] of the experimental results.

4.3.7 Average Desorption Energies

Finally, in Table 4.2 we report desorption translational energies computed according to Equation 4.14 using the newly fitted experimental reaction probability curves. We also computed the average desorption energy for the BOSS model. Since reaction probability curves for a large set of rovibrational states are required in order to estimate this quantity, it has not been possible to evaluate it for the AIMD calculations. Experimental

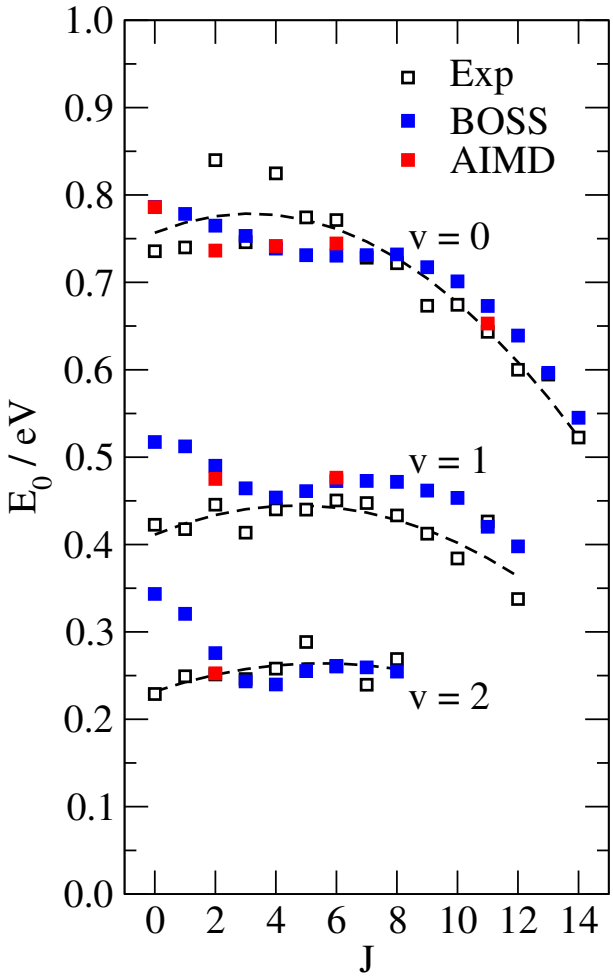

Figure 4.13: Experimental (empty squares) and theoretical (blue and red for BOSS and AIMD, respectively) E_0 values are plotted as a function on J. E_0 values have been estimated from FPC fits of the BOSS data and from LGS fits of the AIMD data. The dashed lines are quadratic fits of the experimental E_0 values, for $v = 0, 1$ and 2 as indicated in the figure.

	$\langle E_{trans} \rangle$
Exp. - Original ERF Fit [13] (T_s = 925 K)	0.559
Exp. - Original ERF Fit [13] (T_s = 925 K, but W from T_s = 120 K)	0.618
Exp. - New LGS Fit (T_s = 925 K)	0.572
Exp. - Comsa&David [64] (T_s = 1000 K)	0.63
Theory - BOSS	0.71

Table 4.2: Experimental and theoretical (BOSS) desorption energies (eV) averaged over D_2 rovibrational states.

desorption energies are now in somewhat better agreement with the value reported by Comsa and David [64]. The value computed from the BOSS reaction probabilities is larger than both experimental values. Experiments, however, were performed at high surface temperature, while a static ideal surface (0 K) characterizes the BOSS calculations. As discussed by Sementa et al. [65], the average desorption energy estimated from reaction probability curves measured at high surface temperature is lower than what would be estimated using low surface temperature reaction probability curves, due to the larger width of the curves at high surface temperature. Specifically, the effect of using the experimental reaction probability curves determined for T_s = 120 K [13] when calculating the average desorption energy at T_s = 925 K, is an increase in the average desorption energy of about 60 meV (see Table 4.2). If we assume that a similar correction might apply to the average desorption energy computed from BOSS data in order to account for surface temperature effects, the agreement of theory (0.71 – 0.06 = 0.65 eV) with the experimental value from Comsa and David [64] (0.63 eV) would be significantly improved.

4.4 Summary and Conclusions

In the present study, the raw associative desorption data from which the experimental initial-state-selected reaction probabilities for D_2 on Cu(111) were extracted [13] have been re-analyzed. In addition, we present new AIMD calculations for this system, in which the reaction probability has been calculated for various initial states simulating the high experimental surface temperature. We also present time-of-flight spectra simulated

from theory, which allow a more direct comparison with the raw experimental data.

Results show that the saturation value of the experimental reaction probability curves is strongly influenced by the functional form employed in the fits. This conclusion might apply to other systems, given that in many studies the reaction probability has been modeled with the ERF form (see Section 4.2.3). The use of the LGS expression, which can assume either a symmetric or non-symmetric shape around the inflection point, suggests similar saturation values for $v = 0, 1$ and 2, in contrast to what was observed earlier with the ERF form. Furthermore, a general trend according to which the degree of symmetry of the reaction probability curves increases with vibrational state is observed. This suggests that the barrier distribution dynamically sampled by the reacting molecules does not have the same shape for the three vibrational states, and that the width of the reaction probability curve is significantly smaller for vibrationally excited molecules ($v = 1, 2$) than for molecules in the ground state. The newly fitted reaction probability curves are closer to the theoretical ones in the onset of the curves and in the saturation values.

The use of a time-of-flight intensity expression that takes into account the longer flight of molecules leaving the surface in an off-normal direction results in a systematic shift of about 40 meV of the fitted reaction probability curves towards higher collision energies. This shift is relevant for the assessment of the accuracy of theoretical models, given that the 'target' chemical accuracy is defined as the ability of modeling an experimental observable within a shift of 1 kcal/mol (≈43 meV). The agreement between theory and experiment, evaluated in terms of energy difference between the theoretical and experimental E_0 values, is now significantly improved: the mean absolute error for the BOSS and AIMD models is now 0.745 kcal/mol (about 50% lower than in Ref. [39]) and 0.594 kcal/mol, respectively, which means that both models now achieve a chemically accurate description of E_0.

The AIMD model slightly improves the agreement between theory and experiment: reaction probability curves are slightly broader and slightly shifted to lower energies, compared to previous BOSS calculations. These findings are consistent with surface

temperature effects. However, theory predicts less broadening of the reaction probability curve with increasing surface temperature than experiment, where the 925 K reaction probability curves are considerably broader than the 120 K ones. Furthermore, even though a larger saturation value is suggested by our reanalysis of the $v = 0$ and $v = 2$ experimental reaction probability curves, theory still gives larger values than experiment for the reaction probability at high collision energies, for all vibrational states, meaning that discrepancies persist between theoretical models and experiments.

4.A Appendix

This appendix contains the barrier heights and geometries in the SRP-PES for high symmetry impact sites (Table 4.A.1); BOSS and AIMD reaction probability curve fitting results (Table 4.A.2 and 4.A.3 and Figures 4.A.1 and 4.A.2); experimental TOF spectra fitting parameters (Table 4.A.4); AIMD reaction probability curve fitting results in which the saturation values of the AIMD fits have been constrained to the corresponding values from the BOSS fits (Figure 4.A.3); W parameters computed for ERF experimental reaction probability curves (Figure 4.A.4); E_0', W' and ν parameters computed for LGS experimental reaction probability curves (Figure 4.A.5); W, W_1 and W_2 parameters computed for LGS experimental reaction probability curves (Figure 4.A.6); adsorption experiment fits plotted on a linear scale (Figure 4.A.7).

Configuration	r (Å)	Z (Å)	E_b (eV)
bth	1.032	1.164	0.628
ttb	1.397	1.386	0.891
fcc, $\varphi = 0°$	1.588	1.270	1.013
t2f, $\varphi = 0°$	1.270	1.270	0.770

Table 4.A.1: Barrier heights and barrier geometries for some configurations in the SRP-DFT PES [39, 40]. The configurations are bridge-to-hollow (bth), top-to-bridge (ttb), above the fcc site (fcc), and above the site midway between a top and fcc site (t2f).

State	Function	A	E_0'	W'	ν	E_0''	W''	χ^2
$v = 0, J = 0$	ERF	0.549	0.808	0.122	-	-	-	546.459
	LGS	0.662	0.792	0.113	$3.69\ 10^{-7}$	-	-	69.560
	FPC	1.000	0.723	0.077	-	0.914	0.228	5.963
$v = 0, J = 2$	ERF	0.503	0.776	0.143	-	-	-	1093.929
	LGS	0.598	0.756	0.128	$4.85\ 10^{-7}$	-	-	226.596
	FPC	0.699	0.635	0.066	-	0.832	0.144	7.208
$v = 0, J = 4$	ERF	0.534	0.762	0.160	-	-	-	1014.269
	LGS	0.642	0.741	0.144	$1.64\ 10^{-7}$	-	-	144.116
	FPC	1.000	0.653	0.099	-	0.911	0.292	3.331
$v = 0, J = 6$	ERF	0.520	0.750	0.124	-	-	-	2858.227
	LGS	0.604	0.728	0.114	$7.96\ 10^{-7}$	-	-	585.047
	FPC	0.896	0.639	0.064	-	0.875	0.206	7.756
$v = 0, J = 11$	ERF	0.594	0.714	0.187	-	-	-	1611.941
	LGS	0.718	0.691	0.171	$3.10\ 10^{-7}$	-	-	265.116
	FPC	0.691	0.481	0.066	-	0.746	0.123	34.501
$v = 1, J = 2$	ERF	0.672	0.562	0.154	-	-	-	6179.267
	LGS	0.712	0.517	0.119	$1.15\ 10^{-7}$	-	-	2099.695
	FPC	0.777	0.518	0.177	-	0.395	0.018	62.617
$v = 1, J = 6$	ERF	0.711	0.537	0.149	-	-	-	5510.366
	LGS	0.752	0.495	0.118	$1.13\ 10^{-7}$	-	-	977.690
	FPC	0.808	0.476	0.180	-	0.406	0.035	70.940
$v = 2, J = 2$	ERF	0.754	0.381	0.178	-	-	-	6301.884
	LGS	0.782	0.328	0.130	$7.24\ 10^{-7}$	-	-	1626.766
	FPC	0.869	0.261	0.080	-	0.248	0.287	78.902

Table 4.A.2: Fit parameters corresponding to the BOSS reaction probability curves plotted in Figure 4.A.1. E_0', E_0'', W' and W'' parameters are in eV.

State	# Data	Function	A	E_0	W'	ν	χ^2
$v = 0, J = 0$	5	ERF	0.673	0.853	0.209	-	10.673
		LGS	0.833	0.832	0.193	$2.04\ 10^{-7}$	4.055
$v = 0, J = 2$	5	ERF	0.587	0.775	0.192	-	6.275
		LGS	0.737	0.761	0.180	$1.70\ 10^{-7}$	3.327
$v = 0, J = 4$	6	ERF	0.638	0.790	0.192	-	7.331
		LGS	0.669	0.773	0.110	0.434	5.037
$v = 0, J = 6$	5	ERF	0.617	0.793	0.204	-	2.427
		LGS	0.745	0.770	0.174	$3.79\ 10^{-7}$	0.886
$v = 0, J = 11$	5	ERF	0.734	0.746	0.265	-	1.405
		LGS	0.917	0.726	0.235	$1.25\ 10^{-5}$	0.111
$v = 1, J = 2$	5	ERF	0.596	0.511	0.159	-	11.912
		LGS	0.665	0.475	0.130	$5.67\ 10^{-7}$	2.435
$v = 1, J = 6$	5	ERF	0.655	0.522	0.175	-	7.356
		LGS	0.753	0.493	0.140	0.002	2.707
$v = 2, J = 2$	5	ERF	0.662	0.326	0.177	-	2.202
		LGS	0.713	0.293	0.124	0.116	0.088

Table 4.A.3: Fit parameters corresponding to the AIMD reaction probability curves plotted in Figure 4.A.2. E_0' and W' parameters are in eV.

State	Dataset	Function	E_0'	W'	ν	χ^2
$v = 0, J = 0$	DS0609A	ERF	0.660	0.171	-	$1.166\ 10^{10}$
		LGS	0.713	0.186	0.050	$5.471\ 10^{9}$
$v = 0, J = 2$	DS0609E	ERF	0.696	0.182	-	$2.647\ 10^{9}$
		LGS	0.785	0.229	$3.67\ 10^{-7}$	$5.759\ 10^{8}$
$v = 0, J = 4$	DS0608D	ERF	0.760	0.199	-	$1.130\ 10^{9}$
		LGS	0.853	0.230	0.055	$4.744\ 10^{8}$
$v = 0, J = 6$	DS0606E	ERF	0.724	0.176	-	$8.276\ 10^{8}$
		LGS	0.757	0.162	0.136	$5.626\ 10^{8}$
$v = 0, J = 11$	DS0607A	ERF	0.617	0.180	-	$4.297\ 10^{11}$
		LGS	0.705	0.228	$1.35\ 10^{-5}$	$3.875\ 10^{11}$
$v = 1, J = 2$	DS0620E	ERF	0.468	0.169	-	$1.750\ 10^{12}$
		LGS	0.454	0.096	0.461	$1.358\ 10^{12}$
$v = 1, J = 6$	DS0620C	ERF	0.483	0.178	-	$2.317\ 10^{12}$
		LGS	0.462	0.094	0.518	$1.917\ 10^{12}$
$v = 2, J = 2$	DS0624D	ERF	0.266	0.145	-	$1.724\ 10^{14}$
		LGS	0.258	0.057	1.000	$1.493\ 10^{14}$

Table 4.A.4: Fit parameters corresponding to the curves plotted in Figure 4.6 obtained in a specific experiment, as indicated by the name of the corresponding data set. E_0' and W' parameters are in eV.

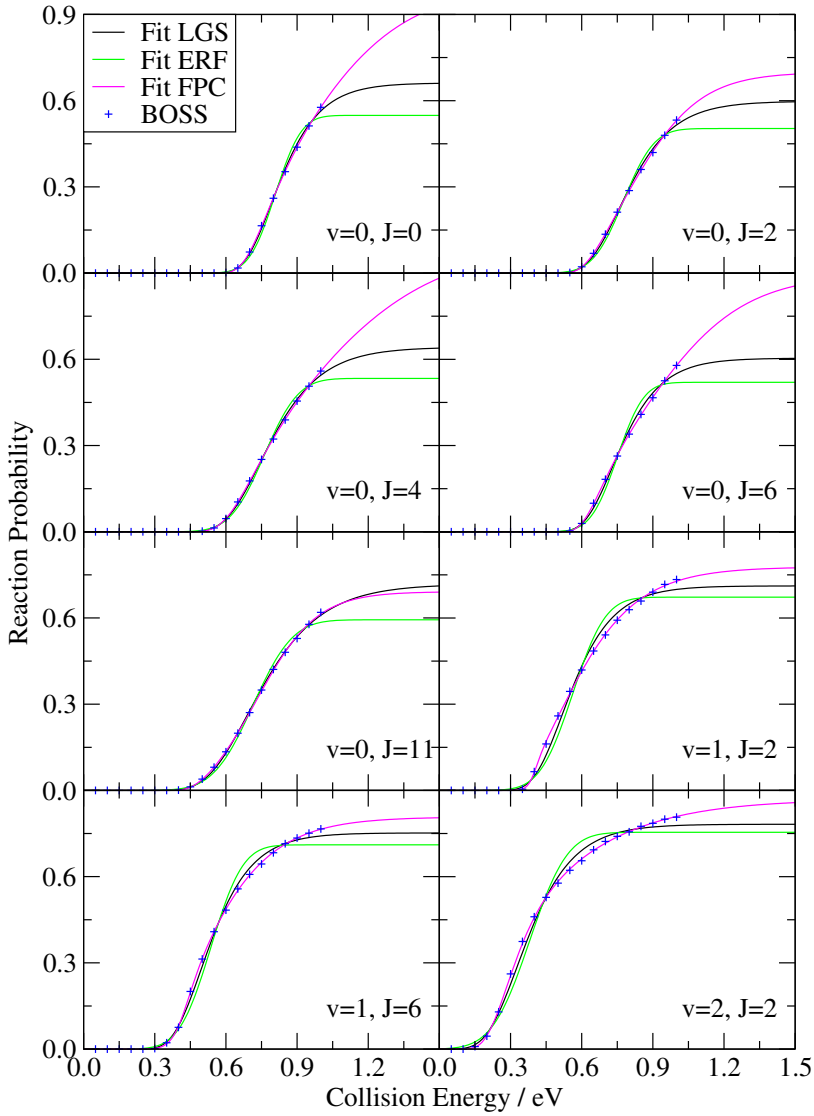

Figure 4.A.1: BOSS reaction probabilities (blue symbols) are plotted as a function of the collision energy for some representative initial states. ERF, LGS and FPC fits of the BOSS data are plotted as green, black and violet solid lines, respectively.

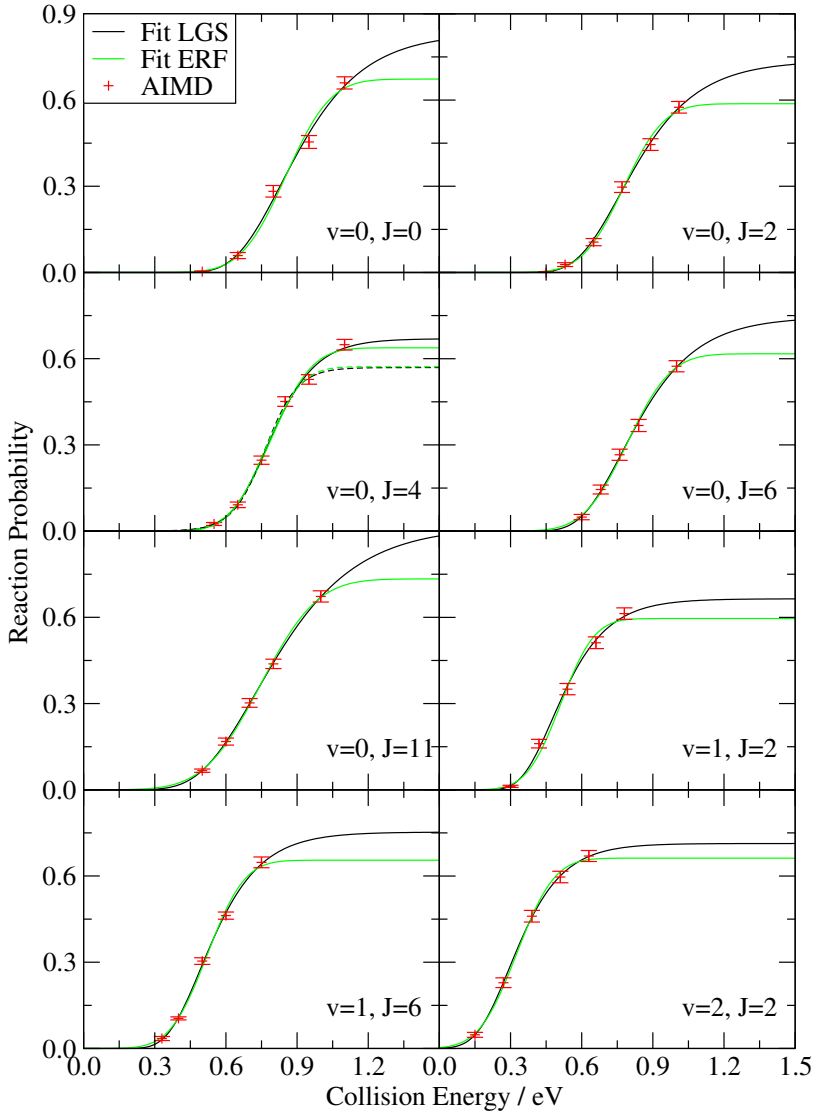

Figure 4.A.2: AIMD reaction probabilities (red symbols) are plotted as a function of the collision energy for some representative states. ERF and LGS fits of the AIMD data are plotted as green and black lines, respectively. For $(v = 0, J = 4)$, also the ERF and LGS fits of the 5 lowest collision energy points are plotted as dashed lines (see text, Section 4.3.2).

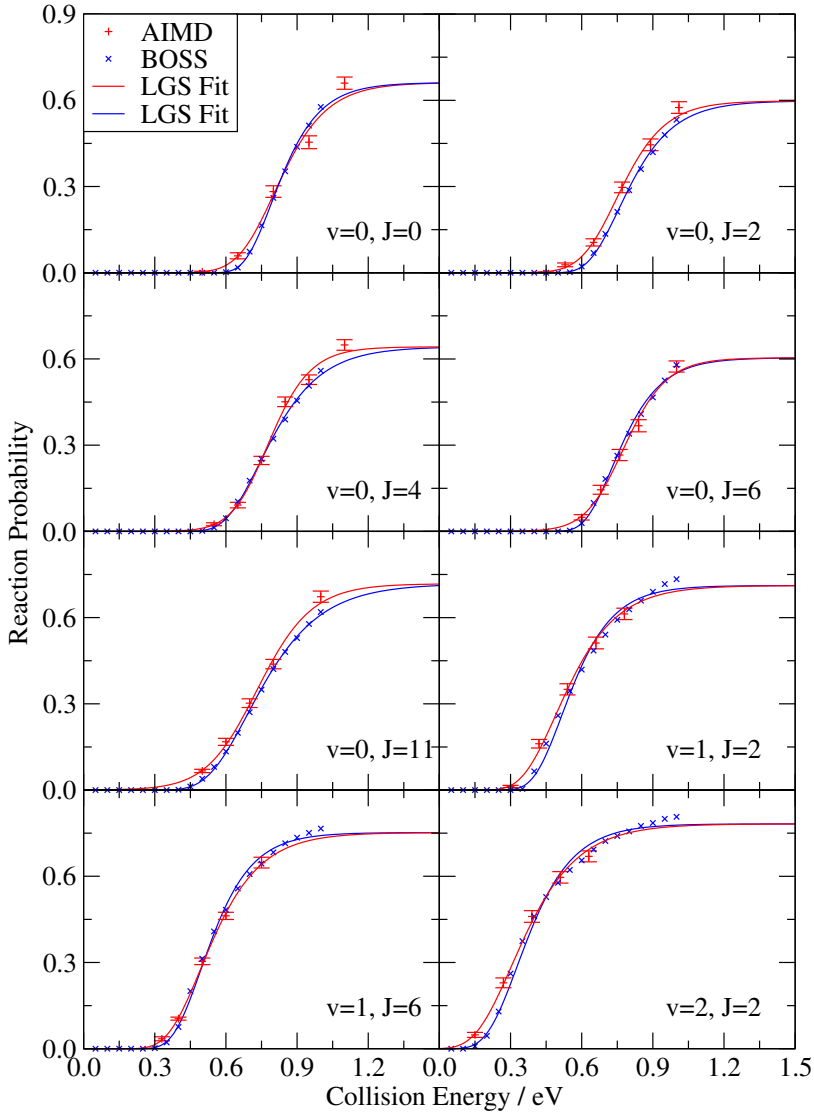

Figure 4.A.3: BOSS and AIMD reaction probabilities (blue × and red +, respectively) are plotted as a function of the collision energy for some representative initial states; the solid lines are LGS fits of the probabilities. The fits of the AIMD data have been constrained to have the same saturation values as the BOSS fits.

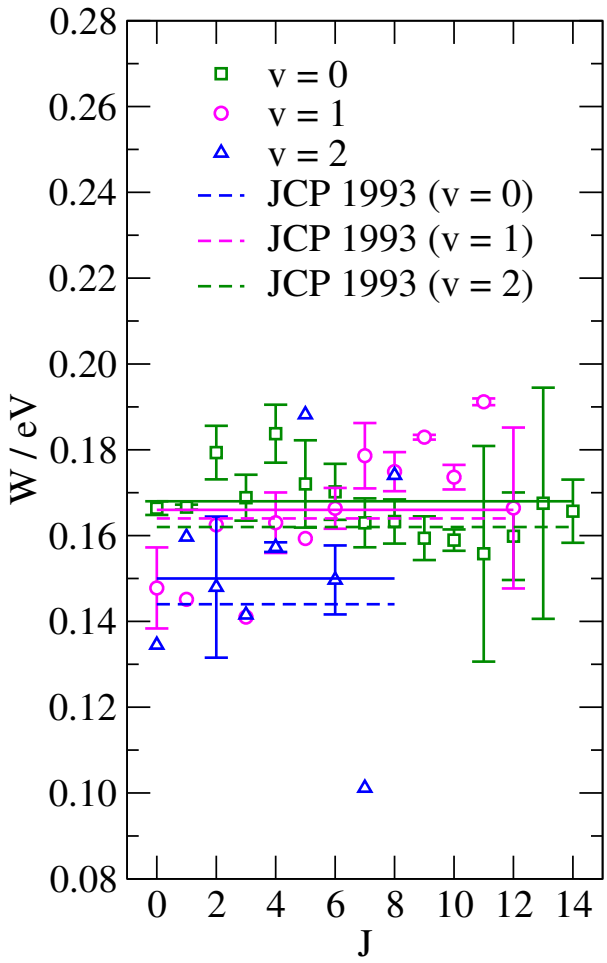

Figure 4.A.4: W parameters obtained from ERF fits of all the available desorption TOF spectra are plotted as a function of the initial rotational state J. Green, violet and blue symbols correspond to $v = 0, 1$ and 2 initial vibrational states, respectively. Solid curves represent average of the $v = 0, 1, 2$ data, while dashed lines are average of the data from Ref. [13]. Line colors are as for the symbols.

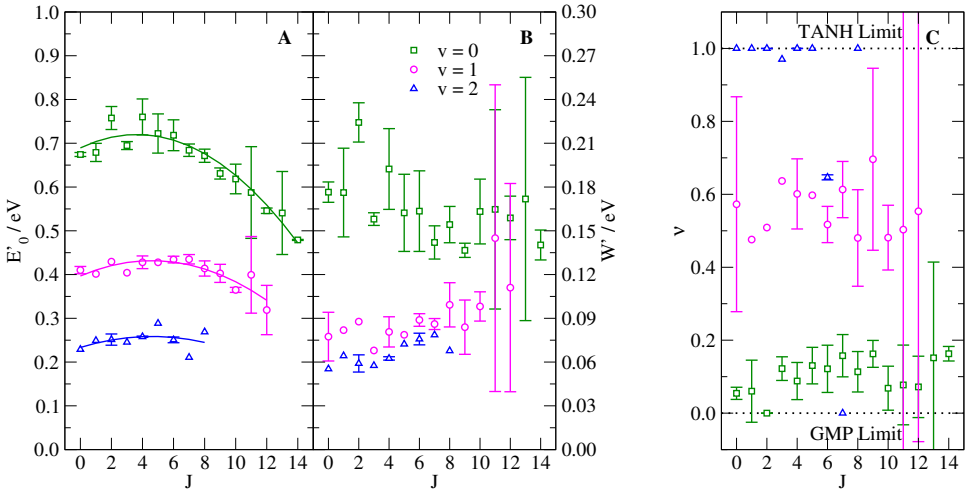

Figure 4.A.5: Parameters obtained from LGS fits of all the available desorption TOF spectra are plotted as a function of the initial rotational state J. Green squares, violet circles and blue triangles correspond to $v = 0, 1$ and 2 initial vibrational states, respectively. Solid curves in the E_0' plot represent quadratic fits of the $v = 0, 1, 2$ data (colors as for the symbols).

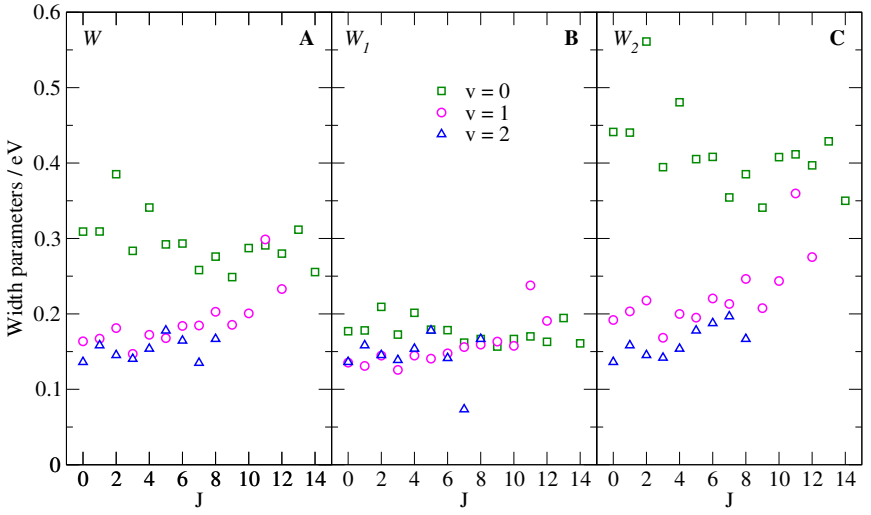

Figure 4.A.6: W, W_1 and W_2 parameters computed for the experimental LGS reaction probability curves are plotted as a function of the initial rotational state J. Green squares, violet circles and blue triangles correspond to $v = 0, 1$ and 2 initial vibrational states, respectively.

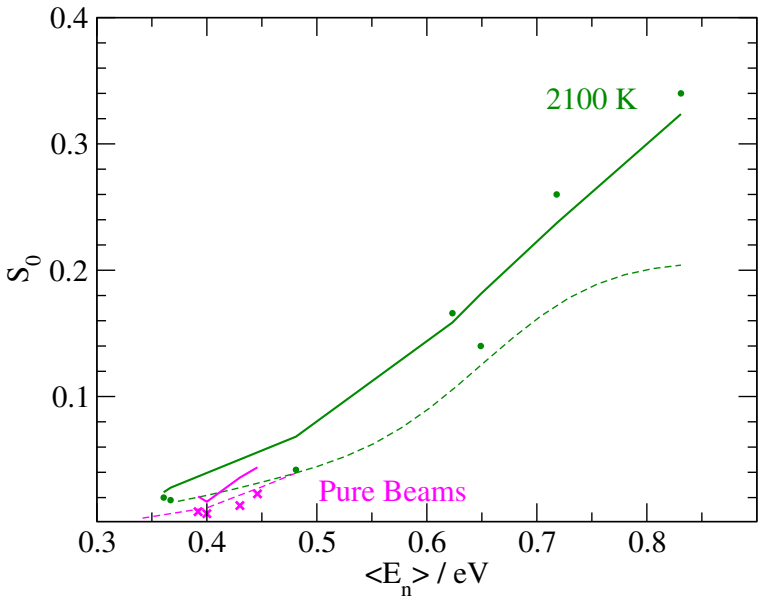

Figure 4.A.7: The sticking probability measured in molecular beam experiments is shown as a function of the average collision energy using a linear scale (only probabilities larger than 1%). Seeded beam results corresponding to specific nozzle temperatures are plotted as circles, pure beam results using crosses. The results of our fits are plotted as solid lines. Dashed lines are from the previous fit (Ref. [13]).

Bibliography

[1] G. J. Kroes, Phys. Chem. Chem. Phys. **14**, 14966 (2012).

[2] P. Nieto, E. Pijper, D. Barredo, G. Laurent, R. A. Olsen, E. J. Baerends, G. J. Kroes, and D. Farías, Science **312**, 86 (2006).

[3] A. C. Luntz and M. Persson, J. Chem. Phys. **123**, 074704 (2005).

[4] J. I. Juaristi, M. Alducin, R. Díez Muiño, H. F. Busnengo, and A. Salin, Phys. Rev. Lett. **100**, 116102 (2008).

[5] G. Anger, A. Winkler, and K. D. Rendulic, Surf. Sci. **220**, 1 (1989).

[6] H. F. Berger, M. Leisch, A. Winkler, and K. D. Rendulic, Chem. Phys. Lett. **175**, 425 (1990).

[7] H. A. Michelsen and D. J. Auerbach, J. Chem. Phys. **94**, 7502 (1991).

[8] A. Hodgson, J. Moryl, P. Traversaro, and H. Zhao, Nature **356**, 501 (1992).

[9] H. A. Michelsen, C. T. Rettner, and D. J. Auerbach, Phys. Rev. Lett. **69**, 2678 (1992).

[10] H. A. Michelsen, C. T. Rettner, and D. J. Auerbach, Surf. Sci. **272**, 65 (1992).

[11] C. T. Rettner, D. J. Auerbach, and H. A. Michelsen, Phys. Rev. Lett. **68**, 1164 (1992).

[12] C. T. Rettner, D. J. Auerbach, and H. A. Michelsen, Phys. Rev. Lett. **68**, 2547 (1992).

[13] H. A. Michelsen, C. T. Rettner, D. J. Auerbach, and R. N. Zare, J. Chem. Phys. **98**, 8294 (1993).

[14] C. T. Rettner, H. A. Michelsen, and D. J. Auerbach, Chem. Phys. **175**, 157 (1993).

[15] C. T. Rettner, H. A. Michelsen, and D. J. Auerbach, Faraday Discuss. **96**, 17 (1993).

[16] C. T. Rettner, H. A. Michelsen, and D. J. Auerbach, J. Chem. Phys. **102**, 4625 (1995).

[17] D. Wetzig, M. Rutkowski, R. David, and H. Zacharias, Europhys. Lett. **36**, 31 (1996).

[18] S. J. Gulding, A. M. Wodtke, H. Hou, C. T. Rettner, H. A. Michelsen, and D. J. Auerbach, J. Chem. Phys. **105**, 9702 (1996).

[19] H. Hou, S. J. Gulding, C. T. Rettner, A. M. Wodtke, and D. J. Auerbach, Science **277**, 80 (1997).

[20] A. Hodgson, P. Samson, A. Wight, and C. Cottrell, Phys. Rev. Lett. **78**, 963 (1997).

[21] M. J. Murphy and A. Hodgson, J. Chem. Phys. **108**, 4199 (1998).

[22] U. Nielsen, D. Halstead, S. Holloway, and J. K. Nørskov, J. Chem. Phys. **93**, 2879 (1990).

[23] G. R. Darling and S. Holloway, J. Chem. Phys. **97**, 734 (1992).

[24] J. Sheng and J. Z. H. Zhang, J. Chem. Phys. **99**, 1373 (1993).

[25] A. Gross, B. Hammer, M. Scheffler, and W. Brenig, Phys. Rev. Lett. **73**, 3121 (1994).

[26] B. Hammer, M. Scheffler, K. W. Jacobsen, and J. K. Nørskov, Phys. Rev. Lett. **73**, 1400 (1994).

[27] A. Forni, G. Wiesenekker, E. J. Baerends, and G. F. Tantardini, Int. J. Quantum Chem. **52**, 1067 (1994).

[28] G. R. Darling and S. Holloway, J. Chem. Phys. **101**, 3268 (1994).

[29] G. R. Darling and S. Holloway, Surf. Sci. **321**, L189 (1994).

[30] G. R. Darling and S. Holloway, Surf. Sci. **307-309**, 153 (1994).

[31] J. Q. Dai, J. Sheng, and J. Z. H. Zhang, J. Chem. Phys. **101**, 1555 (1994).

[32] J. Q. Dai and J. Z. H. Zhang, Surf. Sci. **319**, 193 (1994).

[33] J. Q. Dai and J. Z. H. Zhang, J. Chem. Phys. **102**, 6280 (1995).

[34] A. Forni, G. Wiesenekker, E. J. Baerends, and G. F. Tantardini, J. Phys.: Condens. Matter **7**, 7195 (1995).

[35] J. Q. Dai and J. C. Light, J. Chem. Phys. **107**, 1676 (1997).

[36] J. Q. Dai and J. C. Light, J. Chem. Phys. **108**, 7816 (1998).

[37] M. F. Somers, S. M. Kingma, E. Pijper, G. J. Kroes, and D. Lemoine, Chem. Phys. Lett. **360**, 390 (2002).

[38] S. Nave, D. Lemoine, M. F. Somers, S. M. Kingma, and G. J. Kroes, J. Chem. Phys. **122**, 214709 (2005).

[39] C. Díaz, E. Pijper, R. A. Olsen, H. F. Busnengo, D. J. Auerbach, and G. J. Kroes, Science **326**, 832 (2009).

[40] C. Díaz, R. A. Olsen, D. J. Auerbach, and G. J. Kroes, Phys. Chem. Chem. Phys. **12**, 6499 (2010).

[41] G. J. Kroes, C. Díaz, E. Pijper, R. A. Olsen, and D. J. Auerbach, Proc. Natl. Acad. Sci. U. S. A. **107**, 20881 (2010).

[42] M. Bonfanti, C. Díaz, M. F. Somers, and G. J. Kroes, Phys. Chem. Chem. Phys. **13**, 4552 (2011).

[43] F. Nattino, C. Díaz, B. Jackson, and G. J. Kroes, Phys. Rev. Lett. **108**, 236104 (2012).

[44] M. Wijzenbroek and M. F. Somers, J. Chem. Phys. **137**, 054703 (2012).

[45] A. S. Muzas, J. I. Juaristi, M. Alducin, R. Díez Muiño, G. J. Kroes, and C. Díaz, J. Chem. Phys. **137**, 064707 (2012).

[46] M. Bonfanti, M. F. Somers, C. Díaz, H. F. Busnengo, and G. J. Kroes, Z. Phys. Chem. **227**, 1397 (2013).

[47] S. B. Donald and I. Harrison, J. Phys. Chem. C **118**, 320 (2014).

[48] D. L. Diedrich and J. B. Anderson, Science **258**, 786 (1992).

[49] D. Neuhauser, R. S. Judson, D. J. Kouri, D. E. Adelman, N. E. Shafer, D. A. V. Kliner, and R. N. Zare, Science **257**, 519 (1992).

[50] S. C. Althorpe, F. Fernandez-Alonso, B. D. Bean, J. D. Ayers, A. E. Pomerantz, R. N. Zare, and E. Wrede, Nature **416**, 67 (2002).

[51] S. A. Harich, D. Dai, C. C. Wang, X. Yang, S. D. Chao, and R. T. Skodje, Nature **419**, 281 (2002).

[52] J. C. Juanes-Marcos, S. C. Althorpe, and E. Wrede, Science **309**, 1227 (2005).

[53] S. J. Greaves, E. Wrede, N. T. Goldberg, J. Zhang, D. J. Miller, and R. N. Zare, Nature **454**, 88 (2008).

[54] D. G. Fleming, D. J. Arseneau, O. Sukhorukov, J. H. Brewer, S. L. Mielke, G. C. Schatz, B. C. Garrett, K. A. Peterson, and D. G. Truhlar, Science **331**, 448 (2011).

[55] A. Chakraborty, Y. Zhao, H. Lin, and D. G. Truhlar, J. Chem. Phys. **124**, 044315 (2006).

[56] Y. Y. Chuang, M. L. Radhakrishnan, P. L. Fast, C. J. Cramer, and D. G. Truhlar, J. Phys. Chem. A **103**, 4893 (1999).

[57] E. E. Marinero, C. T. Rettner, and R. N. Zare, Phys. Rev. Lett. **48**, 1323 (1982).

[58] M. Hand and J. Harris, J. Chem. Phys. **92**, 7610 (1990).

[59] H. F. Busnengo, W. Dong, P. Sautet, and A. Salin, Phys. Rev. Lett. **87**, 127601 (2001).

[60] S. J. Klippenstein, V. S. Pande, and D. G. Truhlar, J. Am. Chem. Soc. **136**, 528 (2014).

[61] Ž. Šljivančanin and B. Hammer, Phys. Rev. B **65**, 085414 (2002).

[62] T. Zambelli, J. Wintterlin, J. Trost, and G. Ertl, Science **273**, 1688 (1996).

[63] S. Dahl, A. Logadottir, R. C. Egeberg, J. H. Larsen, I. Chorkendorff, E. Tornqvist, and J. K. Nørskov, Phys. Rev. Lett. **83**, 1814 (1999).

[64] G. Comsa and R. David, Surf. Sci. **117**, 77 (1982).

[65] L. Sementa, M. Wijzenbroek, B. J. van Kolck, M. F. Somers, A. Al-Halabi, H. F. Busnengo, R. A. Olsen, G. J. Kroes, M. Rutkowski, C. Thewes, N. F. Kleimeier, and H. Zacharias, J. Chem. Phys. **138**, 044708 (2013).

[66] K. Gundersen, K. W. Jacobsen, J. K. Nørskov, and B. Hammer, Surf. Sci. **304**, 131 (1994).

[67] M. Karikorpi, S. Holloway, N. Henriksen, and J. K. Nørskov, Surf. Sci. **179**, L41 (1987).

[68] H. E. Pfnür, C. T. Rettner, J. Lee, R. J. Madix, and D. J. Auerbach, J. Chem. Phys. **85**, 7452 (1986).

[69] R. Bisson, M. Sacchi, T. Dang, B. Yoder, P. Maroni, and R. Beck, J. Phys. Chem. A **111**, 12679 (2007).

[70] P. M. Holmblad, J. Wambach, and I. Chorkendorff, J. Chem. Phys. **102**, 8255 (1995).

[71] P. M. Hundt, B. Jiang, M. E. van Reijzen, H. Guo, and R. D. Beck, Science **344**, 504 (2014).

[72] A. Groß and A. Dianat, Phys. Rev. Lett. **98**, 206107 (2007).

[73] A. De Vita, I. Štich, M. J. Gillan, M. C. Payne, and L. J. Clarke, Phys. Rev. Lett. **71**, 1276 (1993).

[74] I. E. Leksina and S. I. Novikova, Sov. Phys-Solid State **5**, 798 (1963).

[75] F. R. Kroeger and C. A. Swenson, J. Appl. Phys. **48**, 853 (1977).

[76] G. Kresse and J. Hafner, Phys. Rev. B **47**, 558 (1993).

[77] G. Kresse and J. Hafner, Phys. Rev. B **49**, 14251 (1994).

[78] G. Kresse and J. Furthmüller, Comput. Mat. Sci. **6**, 15 (1996).

[79] G. Kresse and J. Furthmüller, Phys. Rev. B **54**, 11169 (1996).

[80] G. Kresse and D. Joubert, Phys. Rev. B **59**, 1758 (1999).

[81] J. P. Perdew, K. Burke, and M. Ernzerhof, Phys. Rev. Lett. **77**, 3865 (1996).

[82] J. P. Perdew, K. Burke, and M. Ernzerhof, Phys. Rev. Lett. **78**, 1396 (1997).

[83] J. P. Perdew, J. A. Chevary, S. H. Vosko, K. A. Jackson, M. R. Pederson, D. J. Singh, and C. Fiolhais, Phys. Rev. B **48**, 4978 (1993).

[84] J. P. Perdew, J. A. Chevary, S. H. Vosko, K. A. Jackson, M. R. Pederson, D. J. Singh, and C. Fiolhais, Phys. Rev. B **46**, 6671 (1992).

[85] A. Mondal, M. Wijzenbroek, M. Bonfanti, C. Díaz, and G. J. Kroes, J. Phys. Chem. A **117**, 8770 (2013).

[86] E. B. Wilson, J. Am. Statist. Assoc. **22**, 209 (1927).

[87] T. A. Louis, Am. Stat. **35**, 154 (1981).

[88] A. C. Luntz, J. Chem. Phys. **102**, 8264 (1995).

[89] L. B. F. Juurlink, D. R. Killelea, and A. L. Utz, Prog. Surf. Sci. **84**, 69 (2009).

[90] A. C. Luntz, J. Chem. Phys. **113**, 6901 (2000).

[91] R. A. Olsen, G. J. Kroes, G. Henkelman, A. Arnaldsson, and H. Jónsson, J. Chem. Phys. **121**, 9776 (2004).

[92] J. Harris, Surf. Sci. **221**, 335 (1989).

[93] K. Levenberg, Q. Appl. Math. **2**, 164 (1944).

[94] D. Marquardt, J. Soc. Ind. Appl. Math. **11**, 431 (1963).

[95] J. J. Moré, D. C. Sorensen, K. E. Hillstrom, and B. S. Garbow, The MINPACK Project, in *Sources and Development of Mathematical Software*, edited by W. J. Cowell, pages 88–111, Prentice-Hall, Englewood Cliffs, 1984.

[96] J. J. Moré, B. S. Garbow, and K. E. Hillstrom, User Guide for MINPACK-1, Report ANL-80-74, Argonne, 1980.